New Jersey Institute of Technology
Digital Commons @ NJIT

Theses | Theses and Dissertations

Fall 1994

A high temperature pressure sensor based on magnetic coupling and silicon wafer bonding

Deguang Zhu
New Jersey Institute of Technology

Follow this and additional works at: https://digitalcommons.njit.edu/theses

Part of the Other Physics Commons

Recommended Citation
Zhu, Deguang, "A high temperature pressure sensor based on magnetic coupling and silicon wafer bonding" (1994). *Theses*. 1209.
https://digitalcommons.njit.edu/theses/1209

This Thesis is brought to you for free and open access by the Theses and Dissertations at Digital Commons @ NJIT. It has been accepted for inclusion in Theses by an authorized administrator of Digital Commons @ NJIT. For more information, please contact digitalcommons@njit.edu.

Copyright Warning & Restrictions

The copyright law of the United States (Title 17, United States Code) governs the making of photocopies or other reproductions of copyrighted material.

Under certain conditions specified in the law, libraries and archives are authorized to furnish a photocopy or other reproduction. One of these specified conditions is that the photocopy or reproduction is not to be "used for any purpose other than private study, scholarship, or research." If a, user makes a request for, or later uses, a photocopy or reproduction for purposes in excess of "fair use" that user may be liable for copyright infringement,

This institution reserves the right to refuse to accept a copying order if, in its judgment, fulfillment of the order would involve violation of copyright law.

Please Note: The author retains the copyright while the New Jersey Institute of Technology reserves the right to distribute this thesis or dissertation

Printing note: If you do not wish to print this page, then select "Pages from: first page # to: last page #" on the print dialog screen

NJIT
New Jersey's Science & Technology University

The Van Houten library has removed some of the personal information and all signatures from the approval page and biographical sketches of theses and dissertations in order to protect the identity of NJIT graduates and faculty.

ABSTRACT

A HIGH TEMPERATURE PRESSURE SENSOR BASED ON MAGNETIC COUPLING AND SILICON WAFER BONDING

by
Deguang Zhu

In this thesis, the design and fabrication of a bulk micromachined and wafer bonded pressure sensor for high temperature applications is described. The device design is based on the magnetic coupling principle as described by the Biot-Savart law. By combining the mechanical properties of single crystal silicon with magnetic coupling, the designed sensor can be operated up to 600°C. The key components within the sensor are two inductive coils, a silicon diaphragm and a hermetic vacuum cavity.

The modeling based on a nine-turn single level coil device and a 300 μm × 300 μm diaphragm indicates an output rms voltage range of 70 mV with an input current of 100 mA and frequency of 200 MHz at pressures ranging from 0 kPa to 300 kPa for a sensitivity of 11 μV/mA·MHz·kPa at 300°C. The output voltage doubles to 150 mV at 600 °C for the same pressure range. Experiments on 6-turn single-level aluminum foil coils showed a linear decrease in output with the reduction in coil dimensions as the Young's modulus decreases. Experiments indicate that double-level or multi-level coils give substantially larger output.

The sensor fabrication plan combines standard IC processing, anistropic etch of silicon and silicon wafer bonding. A KOH solution is used to etch the silicon and define the diaphragm. The diaphragm is formed by a boron diffusion technique. The diaphragm thickness is controlled by the diffusion depth and etch-stop technology. The silicon wafer bonding uses sputtered Pyrex as an intermediate adhesive layer. Pyrex has good thermal expansion of coefficient with that of silicon. This would ensure a good thermal match between the silicon and glass together with a good thermal stability at high temperatures.

A HIGH TEMPERATURE PRESSURE SENSOR BASED ON MAGNETIC COUPLING AND SILICON WAFER BONDING

by
Deguang Zhu

A Thesis
Submitted to the Faculty of
New Jersey Institute of Technology
in Partial Fulfillment of the Requirements for the Degree of
Master of Science in Applied Physics

Department of Physics

January 1995

APPROVAL PAGE

A HIGH TEMPERATURE PRESSURE SENSOR BASED ON MAGNETIC COUPLING AND SILICON WAFER BONDING

Deguang Zhu

Dr. William N. Carr, Thesis Advisor — Date
Professor of Physics, NJIT
Professor of Electrical and Computer Engineering, NJIT

Dr. N.M. Ravindra, Committee Member — Date
Associate Professor of Physics, NJIT

Dr. Kenneth Farmer, Committee Member — Date
Assistant Professor of Physics, NJIT

BIOGRAPHY

Author: Deguang Zhu

Degree: Master of Science in Applied Physics

Date: January 1995

Date of Birth:

Place of Birth:

Undergraduate and Graduate Education:

- Master of Science in Applied Physics,
  New Jersey Institute of Technology, NJ, 1995

- Bachelor of Science in Physics,
  Wuhan University, Hubei, China, 1982

Major: Applied Physics

This thesis is dedicated to my parents

ACKNOWLEDGMENT

I wish to express my sincere thanks to Dr. William N. Carr for his valuable and continuing guidance, inspiration, and encouragement during the entire course of this thesis. I also wish to thank Dr. Xiaoyi Gu for his help in mask design. Furthermore, I would like to express my gratitude to all my friends who have made my time in Microelectronics Research Center a memorable one. Especially, I thank Mr. Robert Okojie for his very helpful discussions during the course of this thesis. I am especially indebted to my wife and son for their constant support and encouragement.

TABLE OF CONTENTS

Chapter **Page**

1. INTRODUCTION 1
    1.1 Brief Review 1
    1.2 Objective of this Thesis 2
    1.3 Chapter Synopsis 6
2. PHYSICAL DESCRIPTION OF THE SENSOR DEVICE 7
3. REALIZATION OF A HIGH TEMPERATURE PRESSURE SENSOR 10
    3.1 Voltage Transformer 10
    3.2 Realization of a High Temperature Pressure Sensor 10
    3.3 Sensor Operation 12
4. MAGNETIC MODELING OF THE SENSOR DEVICE 13
    4.1 Device Fundamentals-Biot-Savart Law 13
    4.2 Magnetic Flux Linkage with Coil Gap 21
    4.3 Voltage Output Calculation 23
5. MECHANICAL DESIGN OF THE SENSOR DEVICE 26
    5.1 Overview 26
    5.2 Deflection of a Loaded Thin Square Diaphragm-Timoshenko's Theory 26
    5.3 Mechanical Gap as a Function of Pressure 27
6. SENSOR DEVICE DESIGN 30
    6.1 Device Output as a Function of Fluid Pressure 30
        6.1.1 Voltage Response to Fluid Pressure 30
        6.1.2 Device Response Linearity 33
        6.1.3 Output Voltage Sensitivity to Applied Pressure 34
        6.1.4 The Effects of Coil Turns and Coil Pitches on the Output Voltage 37

TABLE OF CONTENTS
(Continued)

Chapter **Page**

6.2 Temperature Effects on the Sensor Performance 41

6.2.1 Temperature Effects on the Stress of the Diaphragm 41

6.2.2 Temperature Effects on Output Voltage 47

7. PHYSICAL DESIGN OF THE SENSOR DEVICE 50

7.1 Handle Wafer Masks Design 50

7.2 Top Wafer Masks Design 51

8. SENSOR FABRICATION 53

8.1 Device Processing Flow 53

8.2 Discussions of Critical Process Steps 53

8.2.1 Silicon Wafer Bonding 53

8.2.2 Backside Etch of Top Silicon Wafer 56

9. EXPERIMENTS ON ALUMINUM FOIL COILS 57

10. CONCLUSION 59

APPENDIX A 60

APPENDIX B 67

REFERENCES 73

LIST OF FIGURES

Figure		Page
1.1	A Typical Piezoresistive Pressure Sensor	3
1.2	A Three Dimensional View of a Ultra-Sensitive Capacitive Pressure Sensor	3
1.3	Cutway View of a Resonant Microbeam	4
1.4	A Two-Level Bulk-Silicon Tunneling-Based Pressure Sensor	5
2.1	Cross Sectional View of MCHTPS Sensor	8
2.2	Schematic Three Dimensional View of the Primary and Secondary Coil	9
2.3	Schematic View of the Magnetic Coupled High Temperature Pressure Sensor	9
3.1	Schematic View of Two Metal Coils Separated by a Gap g	11
4.1	Biot-Savart Set-up	14
4.2	Top View of a Coil with areas s1, s2, and s3 defined	16
4.3	Magnetic Flux Density B(y') Versus Distance From Coil Section y' for Infinity Length Model for Different Gaps	17
4.4	Magnetic Flux versus Mechanical Gaps for a Coil with 6 Turns	22
4.5	Magnetic Flux versus Mechanical Coil Gaps for Different Coils with Different Turns	23
4.6	Voltage Output Vo as a Function of Coil Gap g for Different Coils with Different Turns	25
5.1	Diaphragm Deflection as a Function of Applied Pressure	28
5.2	Coil Gap g versus Applied Pressure P for Different Sized Thin Diaphragm	29
6.1	Output Voltage as a Function of Applied Pressure for a High Temperature Pressure Sensor	33
6.2	The Linearity of the Output Voltage to Applied Pressure Differential	36
6.3	Output Voltage Sensitivity as a Function of Applied Pressure	38
6.4	Output Voltage versus Applied Pressure Differential for Different Coil Turns	39
6.5	The Effect of Coil Pitches on the Output Voltage	40

LIST OF FIGURES
(Continued)

Figure **Page**

6.6 Stress Built-up in Thin Films 42

6.7 Center Stress of the Square Diaphragm Versus Applied Pressure at Different Temperatures 47

6.8 The Effect of Temperature on the Output Voltage 49

9.1 Results on Device Dimension Scaling Experimental 57

A.1 The First Mask for Cavity Definition on Handle Wafer 60

A.2 The Mask for Primary Coil Definition on Handle Wafer 61

A.3 Device Pattern on Handle Wafer after the Primary Coil Mask Processing 62

A.4 Boron Diffusion Mask for the Definition of Diaphragm Area 63

A.5 Secondary Coil Definition Mask 64

A.6 Pattern Layout on the Top Wafer after Secondary Coil Defined 65

A.7 The Pattern Layout of the Whole Device Chip after the Completion of Device Processing 66

LIST OF TABLES

Table **Page**

6.1 Some Properties of Silicides and High Temperature Metals.................................... 44

6.2 Thermal Expansion Characteristics of Silicon and 7740 Pyrex Glass....................... 46

8.1 Basic Properties of Some Glasses for Silicon Fusion Bonding Applications............ 55

CHAPTER 1

INTRODUCTION

1.1 Brief Review

Similar to integrated circuit, sensor and transducer technology has advanced very fast in the past ten years. Used as a mechanical material, silicon has many applications[1–8]. Silicon-based pressure sensors are among the most widely and successfully developed applications in microsensors. Silicon is not only used as mechanical material, but it can also be used as an active electronic component, such as piezoresistor. Transducers for pressure are among the oldest microsensors that are realized in silicon and are devices for which the demand continues to be very high. Specific designs and mounting arrangements very considerably ranging from small, sensitive, catheter-tip transducers used within the heart to the larger, more rugged devices needed for industrial process control. However, in spite of the wide range of applications, only a few approaches dominate development efforts in silicon. Piezoresistive structures have been the traditional basis for such transducers, offering small size, excellent linearity over a wide dynamic range and moderately high pressure sensitivity. These kinds of sensor devices usually include diffused resistors integrated as a Wheatstone Bridge. Figure 1.1 shows the top view of such a typical piezoresistive pressure sensor[2]. The resistors are arranged symmetrically such that one pair of resistors in an opposite position experiences longitudinal stress and the other pair of resistors experiences transverse stress when the diaphragm is deflected by an applied pressure. The stress associated with deflection alters the carrier mobility in the resistors, giving rise to their pressure sensitivity. In this way, pressure is measured. Since these devices normally use the p-n junction for electrical isolation, they, in general, can only be operated at temperatures lower than 150°C. This is because of the intrinsic high temperature sensitivity of the diffused resistors and p-n junctions. An increasingly used

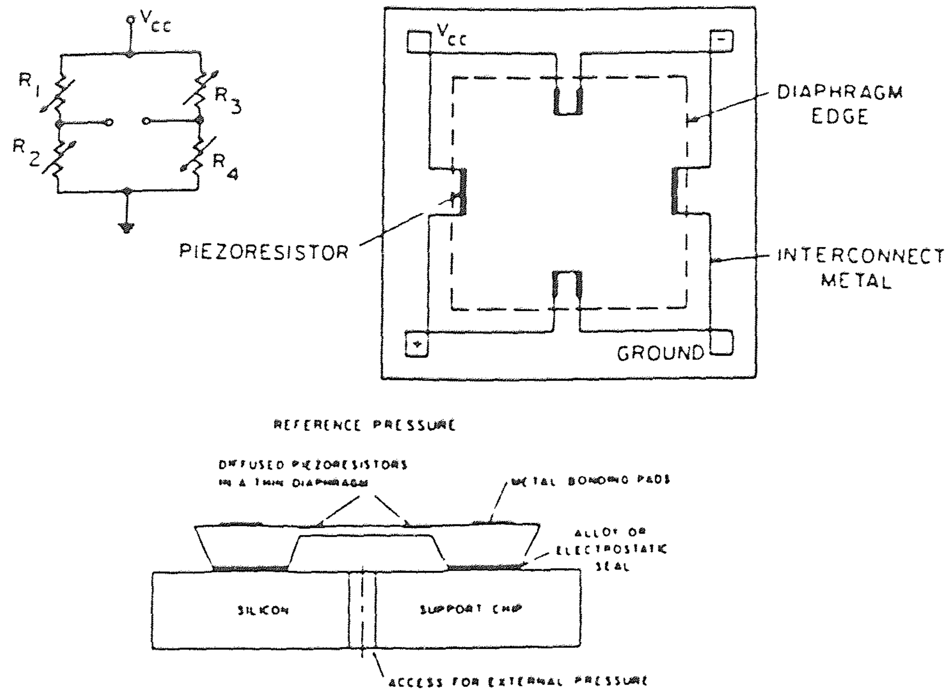

Figure 1.1 A typical piezoresistive pressure sensor [2]

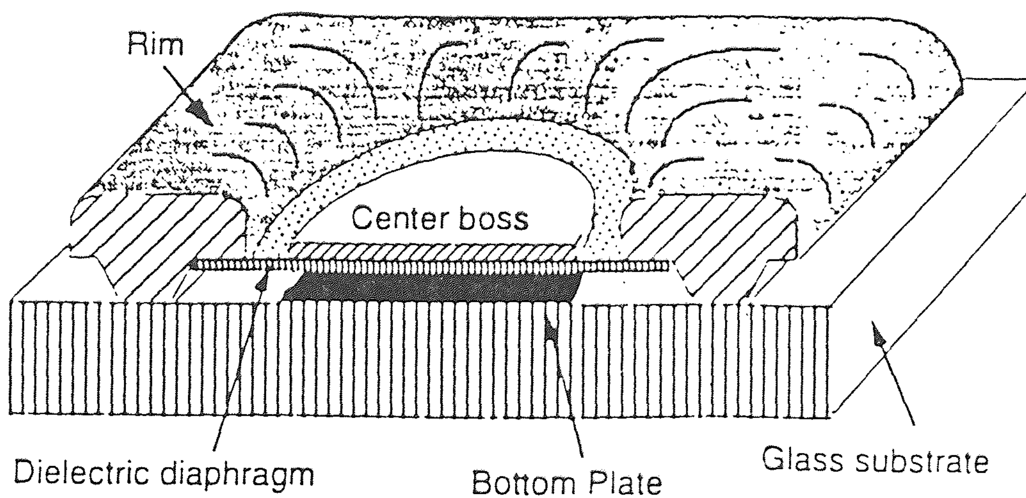

Figure 1.2 A three dimensional view of a ultra-sensitive capacitive pressure sensors [5]

pressure sensor[5] is the capacitive-type device. Figure 1.2 shows a typical capacitive-type pressure sensor in top view. These sensors are typically the traditional parallel-plate capacitor with one diaphragm plate movable under the stress of pressure. These parallel plates are usually glass/silicon or silicon/silicon. As pressure variations move the diaphragm, the sensor's capacitance changes. Pressure is measured through the movement of a diaphragm. A category of pressure sensors are based on the natural resonance of the resonant beam tethered on one end, as shown in figure 1.3[7]. When the pressure is applied, the resonant frequency of the beam changes. The change in resonant frequency reflects the change in pressure. A fourth category of pressure sensors are quantum mechanical tunneling-baseddevices, as shown in figure 1.4[8]. The example sensor is constructed with a tunneling tip supported by a glass substrate and sealed by a silicon diaphragm and the glass substrate. Initially , the beam is deflected up, by applying a static bias voltage between it and diaphragm and producing an electrostatic force, to bring the tip close enough to the counter-electrode on the diaphragm. When an external pressure P is applied the diaphragm deflects, and the tunneling current will change at a constant V. All the above mentioned sensors have their advantages and disadvantages. They all have been designed to operate at temperatures lower than 200 °C, although the tunneling gauge is potentially useful for higher temperatures.

1.2 Objective of This Thesis

To meet the high temperature applications, several papers have reported pressure sensors suitable for temperatures around 350°C[9–13]. However, these reported sensors are basically the modifications of the existing devices such as piezoresistive and capacitive sensors are not applicable at even higher temperatures.

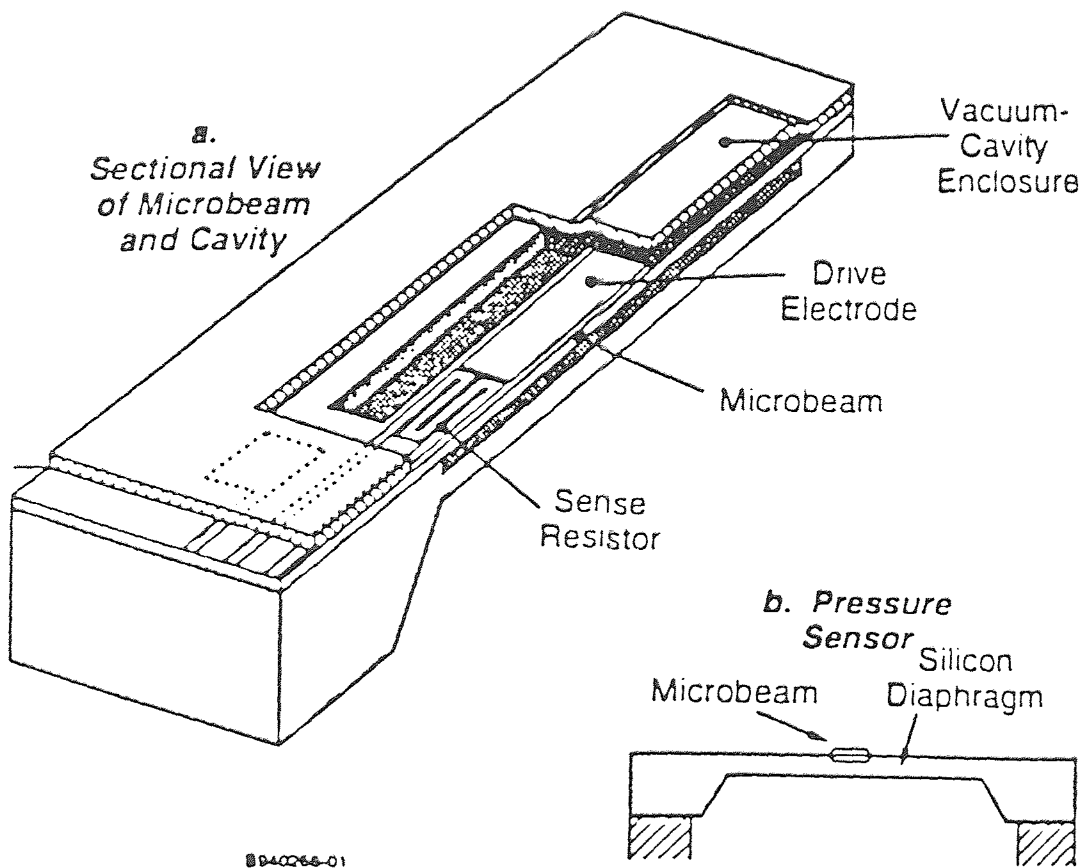

Figure 1.3 Cutway view of a resonant microbeam. The sectional view in (a) shows the microbeam inside its vacuum-cavity enclosure with a central electrode and a position sensing microbeam at one end [7]

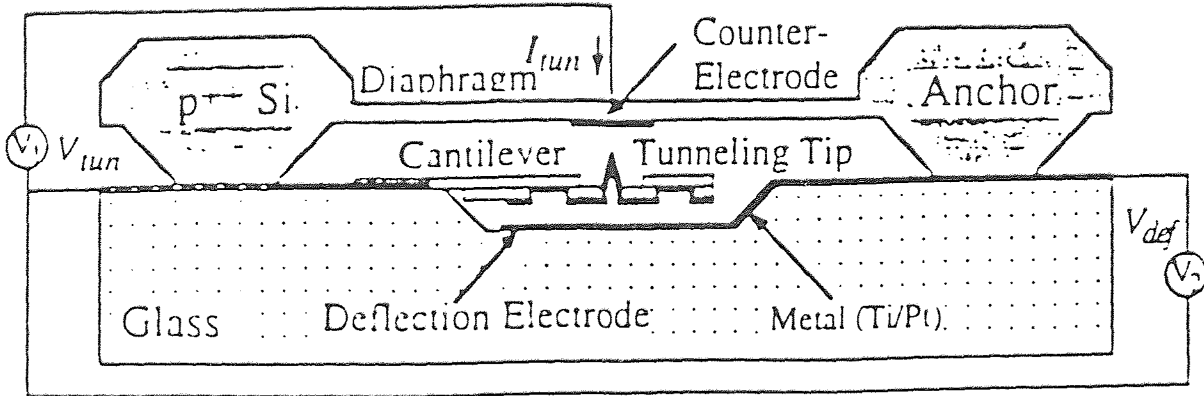

(a)

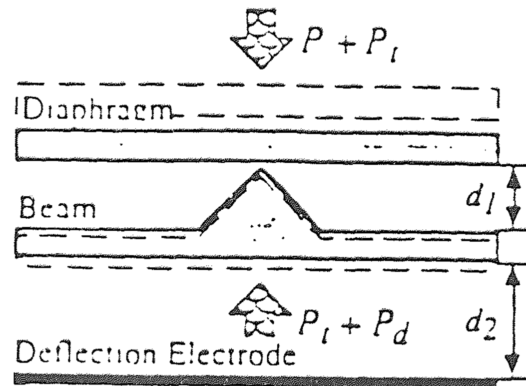

(b)

Figure 1.4 A two-level bulk-silicon tunneling-based pressure sensor [8]

For even higher temperature applications, this thesis describes a device based on magnetic coupling for a new generation of pressure sensors. The device is based on magnetic coupling and transformer actions. Based on this concept we describe the design and fabrication of this new device. Two major steps involved in the device fabrication are wafer bonding and backside etch. There they will be discussed in detail. The active elements are metal inductors which are sealed in a cavity by handle wafer and a cap diaphragm.

1.3 Chapter Synopsis

This thesis includes 10 chapters. Chapter 2 following the introduction in chapter 1 will give a physical description of the sensor device. The principle, design concept and device modeling will be presented in chapters 3 through chapter 6. Chapter 7 through chapter 8 describe the specific design, fabrication of the sensor device. The chapter 9 is experimental data. The final chapter 10 is the conclusion. Key processing steps such as backside etching for diaphragm formation and wafer bonding will be discussed in a more detailed way. The physical masks are included in the Appendices.

CHAPTER 2

PHYSICAL DESCRIPTION OF SENSOR DEVICE

The high temperature sensor described in this thesis adopts a concept based on magnetic coupling. It is constructed with two major parts-a diaphragm and two metal inductive coils. The coils constitute the electrical functioning part and the diaphragm plays the mechanical part of the sensor device. Figure 2.1 shows a cross section view of the sensor device. The primary coil sits in the cavity etched down to the handle wafer, and the secondary coil sits on the boron diffused diaphragm on the top wafer. Both the handle wafer and the top wafer are N-type (100) single crystal silicons. The two coils are sealed in the cavity with one positioned to directly face using silicon wafer bonding technique. With the completion of the etch back of the top wafer, the boron diffused area is retained due to the etching stop at the heavy boron diffused area to create the thin diaphragm. The contact pads for both primary coil and secondary coil are realized by using buffered HF to etch away the Pyrex glass and the oxide layers. Finally the bonded wafer compositeis diced into small discrete chips. In this way, a complete sensor device is realized.

Figure 2.2 shows a three dimensional view of two coils. The top one is the secondary coil and the lower one is the primary coil. The secondary coil is directly above the primary coil. Figure 2.3 shows the three dimensional view of a sensor device. The diaphragm is a boron doped crystalline silicon and is formed by etch stop technique using wet anisotropical etching. A cavity is sealed under the diaphragm at the time of wafer bonding and the final before etch back.

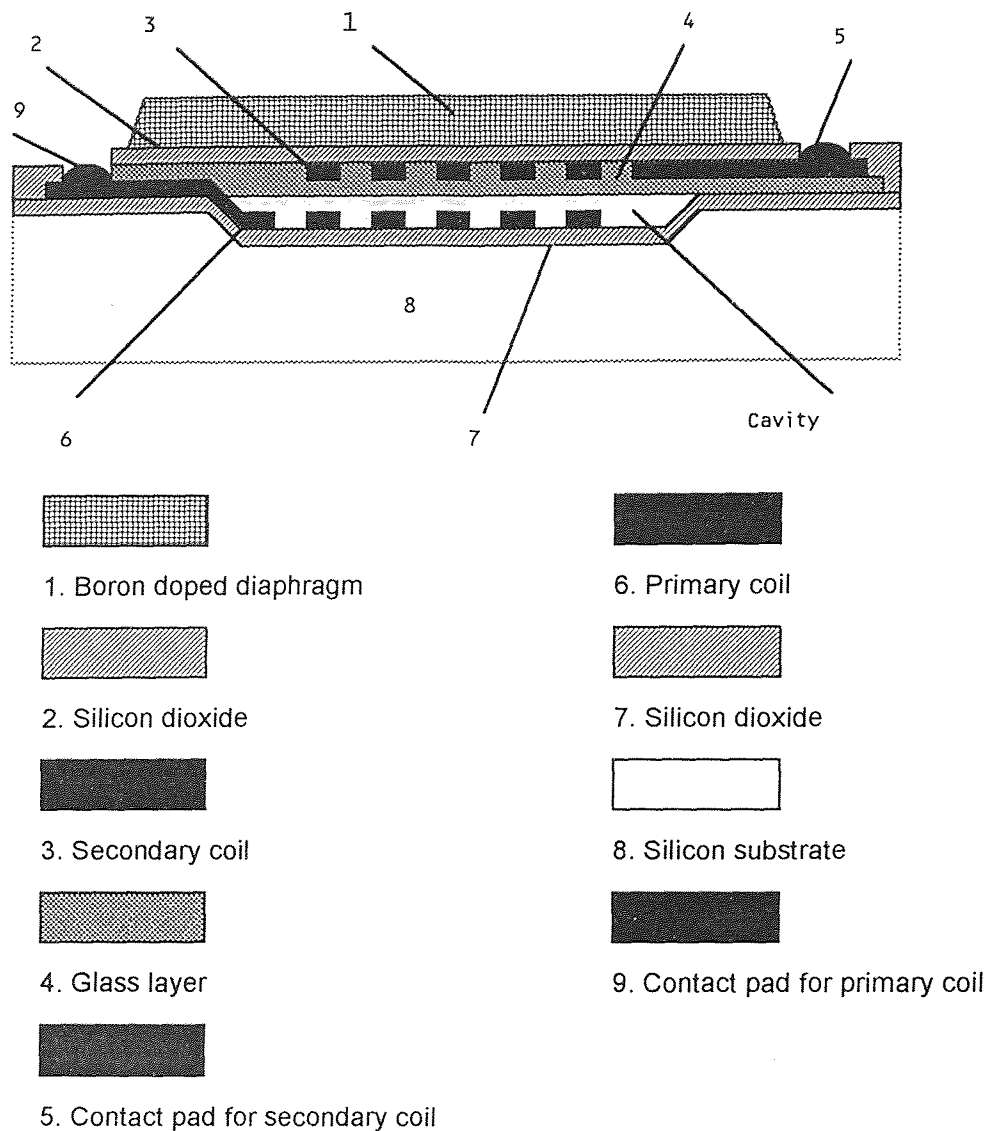

Figure 2.1 Cross sectional view of MCHTPS sensor. (1). silicon diaphragm (2).silicon dioxide (3).secondary coil (4).intermediate glass layer (5).contact pad for secondary coil (6).primary coil (7).silicon dioxide (8).silicon substrate (9).contact for primary coil

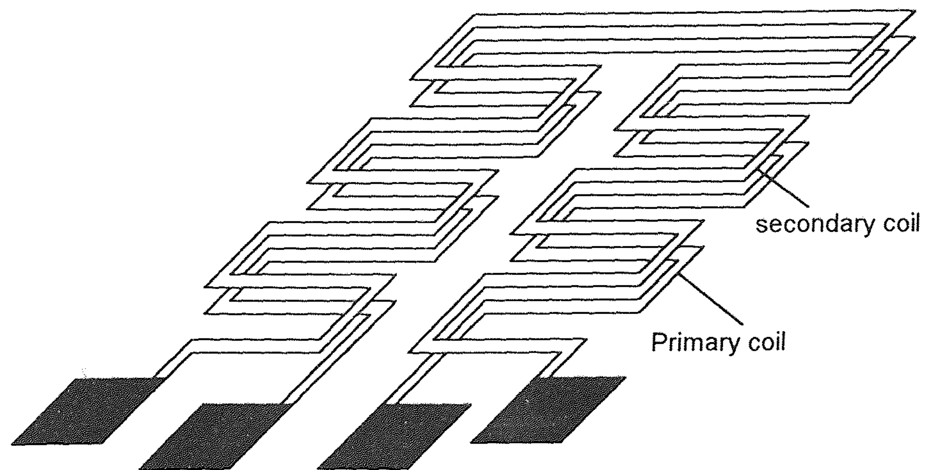

Figure 2.2 Schematic three dimensional view of the primary and secondary coil

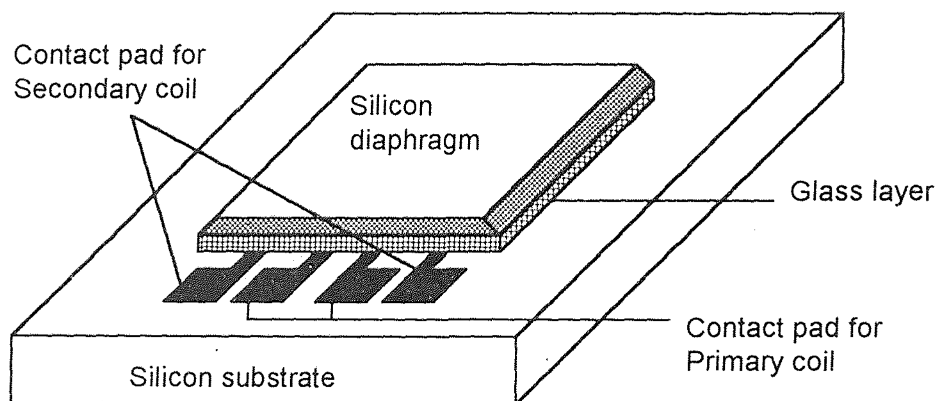

Figure 2.3 Schematic view of the magnetic coupled high temperature pressure sensor

CHAPTER 3

REALIZATION OF A HIGH TEMPERATURE PRESSURE SENSOR

3.1 Voltage Transformer

It is well known from the Biot-Savart law that when two metal coils are brought closer, the alternative current applied to one coil (primary coil) will induce an voltage output in the other coil(secondary coil). The output in the secondary coil depends on the frequency and the amplitude of current in the primary coil as well as the distance between the two coils. This is the magnetic coupling principle. It is utilized in a high temperature pressure sensor in this thesis to link the mechanical and electrical actions. Figure 3.1 shows two coils separated by a distance or gap g. Any change in gap g either mechanically or electrically will result in a change in the induced voltage output in the passive (secondary) coil. Therefore, a voltage transformer is realized. This has been used by OMEGA[13] and others as the basis for a commercial product line of pressure sensors.

3.2 Realization of a High Temperature Pressure Sensor

As mentioned in section 3.1, a voltage transformer was used by OMEGA as pressure sensors. The OMEGA pressure sensor utilized nickel-iron as coil material. This material is not stable at high temperatures. In this thesis, the proposed pressure sensor is made primarily of two metal films vacuum sputtered and IC patterned into coils. From the previous discussion and figure 2.1 and figure 3.1, the two coils are shaped in the exact way, with same size and same turns. One coil is just above another with a gap g. The handle wafer and diaphragm are both made of crystalline silicon. The primary coil lies in a cavity and is isolated from the handle wafer by a thermally grown silicon dioxide layer. The secondary coil sits on the diaphragm and is also isolated by a thermally grown silicon

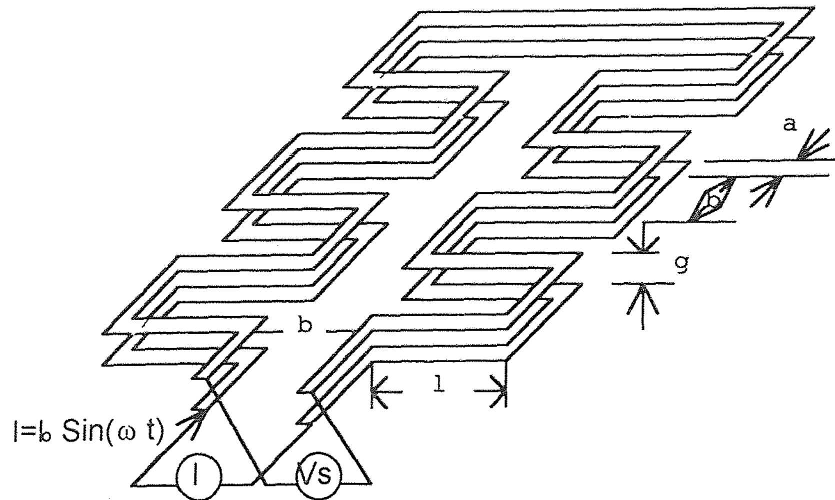

Figure 3.1 Schematic view of two metal coils separated by a gap g.

dioxide layer. Two wafers are bonded through a Pyrex glass(#7740 Corning Glass Company) layer. Output contact pads are automatically revealed with the completion of the diaphragm formation by the wet chemical etching and dip in buffered HF. Two coils are symmetrically arranged. Coil material can be arbitrarily chosen, from aluminum for sensor operation at temperatures around 300°C, to silicides such as tantalum silicide($TaSi_2$), tungsten silicide(WSi_2), platinum silicide($PtSi_2$), and high temperature metals such as palladium and platinum for applications at temperatures above 600°C. In this thesis, $PtSi_2$ is chosen for sensor operations above 600°C. $PtSi_2$ is chosen based on two reasons: 1) $PtSi_2$ is a high temperature material stable at 800 °C, and 2) $PtSi_2$ can be directly wire bonded. This is critical in many circumstances in micromechanical sensor devices which will be discussed later.

Because there is no p-n junction in this sensor and all materials used for the device can withstand high temperature, the pressure sensor can be operated at temperatures above 600°C. The limiting factor is the onset of plastic creep in the silicon itself. Furthermore, the symmetrical arrangement in the sensor design also enhances temperature stability at high temperature applications.

The fabrication of the sensor is firstly to etch out a cavity in the handle wafer by wet anisotropical chemical etching. Alternatively, the top wafer is heavily boron diffused to define the diaphragm area. After a thermal oxide is grown on both handle wafer and top wafer, a metal layer is sputter deposited onto the two wafers. Following this, both primary and secondary coils are patterned. The following step is to deposit a low temperature glass intermediate layer of thickness around 1 μm onto the top wafer. This is done by sputtering. The glass layer thickness is chosen to be thicker than the thickness of two coil metal layers combined together for good bonding. Then the handle wafer and the top wafer are carefully aligned and pressed together, and then treated at 900°C for 15 minutes. The glass selected is Corning 7740 and it has the thermal expansion of 3.4×10^{-6}/K and is close to that of silicon(2.6×10^{-6}/K). Because the coil metal layer is thin compared with the glass layer, the property of this sandwich structure is mainly governed by silicon substrate and the glass layer. This would ensure the thermal stability of the sensor device at high temperatures. The final sensor chip will result after back etch of the top wafer, as shown in figure 2.1.

3.3 Sensor Operation

The pressure sensor described in this thesis operates by the principle of electromagnetic induction. An alternative current passes through the primary coil, generating a magnetic field that creates a flux and an induced voltage in the secondary coil. Upon the application of pressure on the diaphragm, the diaphragm is stressed and the gap between the two coils will change, and therefore changing the induced voltage on the secondary coil. In this way, the change in applied pressure is measured.

CHAPTER 4

MAGNETIC MODELING OF THE SENSOR DEVICE

In the previous chapters, we have presented a physical description of the sensor device. In this chapter, we will describe the principles for sensor device operation.

4.1 Sensor Fundamentals-Biot-Savart Law

When two metal coils are aligned in close proximity with a gap g, a current passing through one coil will induce a voltage output in another coil. This is the well known Biot-Savart electromagnetic induction principle. This lays the foundations for our high temperature pressure sensor. The arrangement of the two coils was shown in figure 2.2 and figure 3.1.

Figure 4.1 shows any straight sections of a coil with origin set at the center of the section of the primary coil. Assuming a line coil model and that the current I passes through the primary coil, the defferential magnetic flux density **dB** produced at any point P in the plane of secondary coil can be expressed as

$$d\bar{B} = \frac{\mu}{4\pi}\frac{Id\bar{l} \times \bar{r}}{r^2} \qquad (4\text{-}1)$$

where μ is the permeability of air and r is distance between current element dI and point P. This is known as Biot-Savart law. $\bar{r}$ is the unit vector and is written as

$$\bar{r} = \frac{\bar{i}(x-x') + \bar{j}(y-y') + \bar{k}(z-z')}{((x-x')^2 + (y-y')^2 + (z-z')^2)^{1/2}} \qquad (4\text{-}2)$$

and

$$d\bar{B} = \frac{\mu I}{4\pi}\frac{\bar{k}(y-y')dx + \bar{j}gdx}{((x-x')^2 + (y-y')^2 + g^2)^{3/2}} \qquad (4\text{-}3)$$

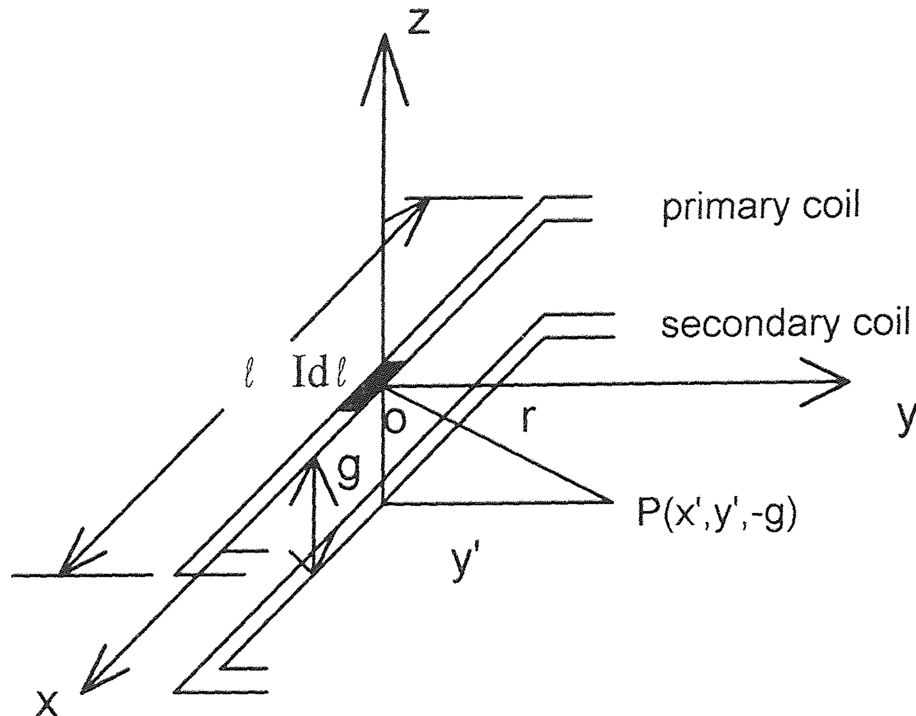

Figure 4.1 Biot-Savart set up

where we have used the fact that dl is along x-direction and z-z'= g. We can see that the magnetic flux density components along x- and y-directions are parallel to the secondary coil plane. They do not contribute to the magnetic flux passing through the secondary coil and therefore do not induce voltage output in the secondary coil. Thus only the component along z-direction contributes to magnetic flux ϕ through secondary coil plane. Therefore, we need to consider only the z-direction component dB_z , i.e.

$$dB_z = \frac{\mu I}{4\pi}\frac{(y-y')dx}{r^3} \tag{4-4}$$

with the above coordinate set-up, y has been chosen equal to 0. The magnetic flux density at any point P(x',y',-g) in the secondary coil can be obtained by integrating dBz in the secondary coil plane with respect to x from -l/2 to +l/2. We have

$$B_z(y') = -\frac{\mu I}{4\pi}\int_{-l/2}^{l/2} y' \frac{dx}{((x-x')^2 + y' + g^2)^{3/2}} \tag{4-5}$$

where l is the length of the coil section concerned. Based on the calculations done by Okojie[33] that the current passing that coil section contributes mainly in the nearest coil area abounding to it, we can use the infinity length model as a first order approximation. By letting $l=\infty$ and integrating with respect to x from $-\infty$ to $+\infty$, we get the magnetic flux density at distance y' from the coil section concerned as

$$B_z(y') = -\frac{\mu I}{4\pi}\frac{2y'}{(y'^2 + g^2)} \tag{4-6}$$

However, a finite length model should be used to get more accurate result. By finishing the integration equation 4-5, we get the magnetic flux density at point P(x',y',-g) as

$$B_z(x',y') = -\frac{\mu I}{4\pi}\frac{y'}{(y'^2+g^2)}\left(\frac{\frac{l}{2}-x'}{((\frac{l}{2}-x')^2+y'^2+g^2)^{1/2}} + \frac{\frac{l}{2}+x'}{((\frac{l}{2}+x')^2+y'^2+g^2)^{1/2}}\right) \tag{4-7}$$

We will neglect the minus sign in equations (4-6) and (4-7) in the following calculations because we are interested only in its magnitude. The magnetic flux in the secondary coil can be obtained by integrating the magnetic flux density expressed in (4-7) over the whole secondary coil plane. The accurate calculation of magnetic flux is not simple because of the edge effect. However, we can reasonably assume that each coil section contributes only to the coil area facing to it. The whole coil can be segmented into different sections. Similar calculations can be done to all sections with the same or different length l. Under this assumption and by referring to figure 4.2, sections AD and ad contributes only

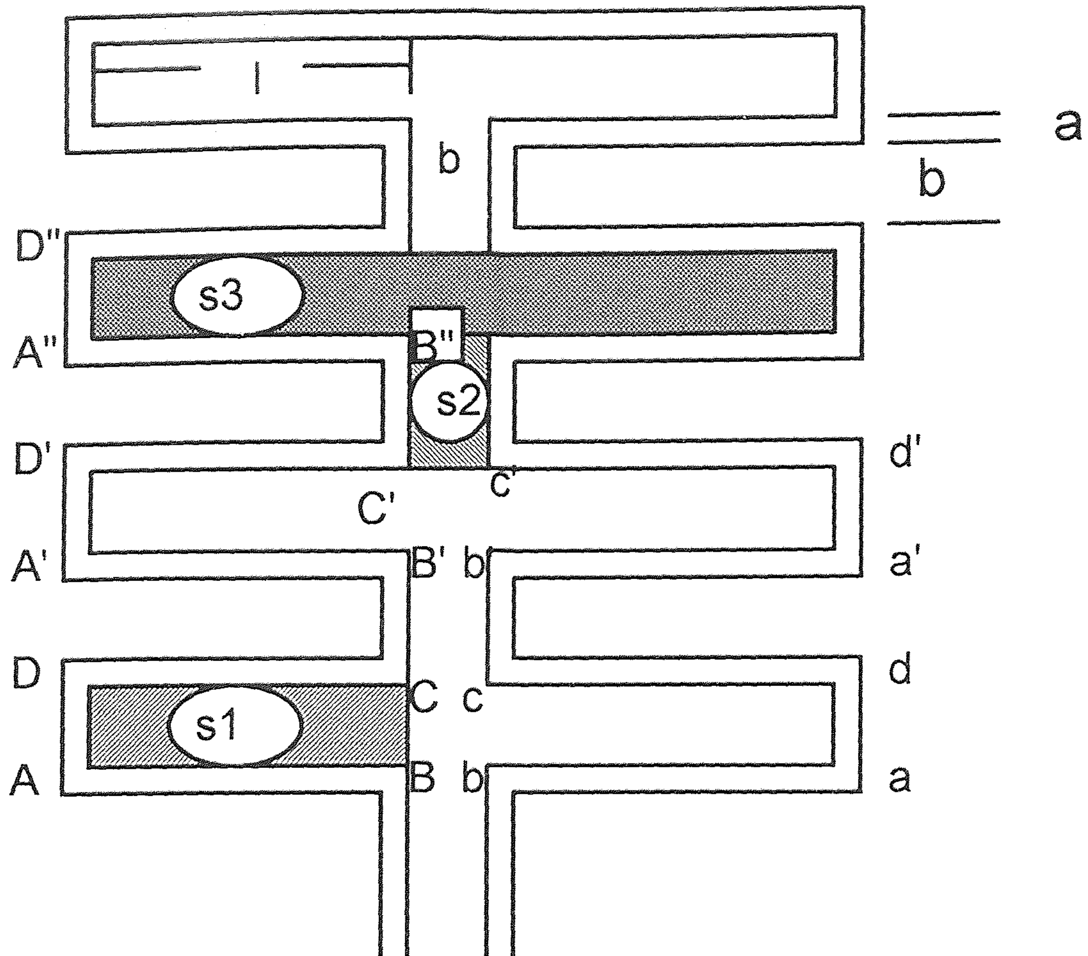

Figure 4.2. Top view of a coil with areas s1, s2, and s3 defined

to area ADda (area s3 equivalent) and section AB contribute only to area s1(equivalent), section B"C' to area s2 (equivalent), etc. By symmetry, we have to consider only half of the coil and multiply by factor 2 later. For simplicity and clearness, we can use the infinity length model to show the variation of the magnetic flux density Bz(y') with the distance y' from the coil section concerned and the gap g. The results are shown in figure 4.3.

We can see that the magnetic flux density decreases quickly with the distance y'. Therefore, as a first order approximation, we can get the magnetic flux Φ in coil.2 plane by simply integrating Bz(y') with respect to x' from -L/2 to +L/2 and y' from 0 to b for infinity length model. The resulting magnetic flux is

$$\Phi = \frac{\mu IL}{4\pi}\ln(\frac{b^2+g^2}{g^2}) \tag{4-8}$$

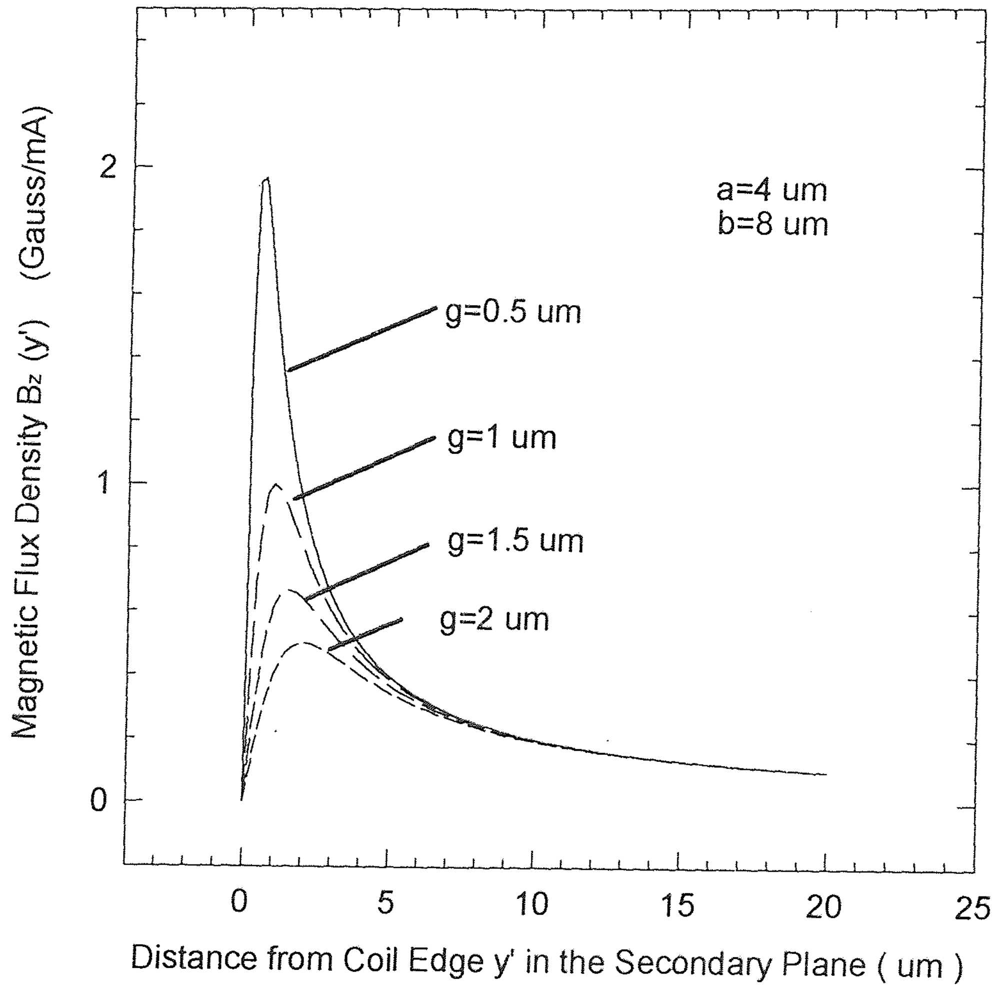

Figure 4.3 Magnetic flux density B(y') versus distance from coil section y' for infinity length model for different gaps

where

L is the total length of the coil

$I = I_0 \sin(\omega t)$ is the applied current in the primary coil

I_0 is the amplitude of the applied current signal

ω is the frequency of the applied current signal

For finite length model, we have to use equation (4-7) to calculate the magnetic flux. With the assumptions mentioned above, the current flowing in the coil section only contributes to the magnetic flux Φ in the area facing to it. For example, coil section AB in figure 4.2 only contributes to Φ in area ABCD (s1), A'B'C'D' and A"B"C"D" , etc. Thus, the magnetic flux in coil area s1 produced by coil section AB is

$$\Phi_1 = \frac{\mu I}{4\pi}\int_{-l/2}^{+l/2} dx' \int_0^b \frac{y'}{y'^2+g^2}\left(\frac{l/2-x'}{((l/2-x')^2+y'^2+g^2)^{1/2}} + \frac{l/2+x'}{(l/2+x')^2+y'^2+g^2)^{1/2}}\right)dy'$$

(4-9)

Finishing the integration with respect to x', the equation (4-9) can be rewritten as

$$\Phi_1 = \frac{\mu I}{2\pi}\int_0^b \frac{y'.(\sqrt{\ell^2+y'^2+g^2} - \sqrt{y'^2+g^2})}{y'^2+g^2}dy' \qquad (4\text{-}10)$$

This integration can only be done in numerical way. Because section CD contributes the same amount to Φ1 in area s1, the above magnetic flux should be multiplied by a factor of 2, i.e.

$$\Phi_1 = \frac{\mu I}{\pi}\int_0^b \frac{y'.(\sqrt{\ell^2+y'^2+g^2} - \sqrt{y'^2+g^2})}{y'^2+g^2}dy' \qquad (4\text{-}11)$$

However, other coil sections parallel to section AB and CD also produce flux in area s1. Let

$$f(y') = \frac{\mu I}{\pi} \frac{y'(\sqrt{\ell^2 + y'^2 + g^2} - \sqrt{y'^2 + g^2})}{y'^2 + g^2} \tag{4-12}$$

the magnetic flux produced in area s1 by the nearest turn is

$$\Phi_2 = \int_{2(a+b)}^{2a+3b} f(y')dy' - \int_{a+b}^{a+2b} f(y')dy' \tag{4-13}$$

The magnetic flux produced in s1 by turn 3, turn 4, turn 5 and turn 6 will be denoted by Φ3, respectively. they are

$$\Phi_3 = \int_{4(a+b)}^{4a+5b} f(y')dy' - \int_{3(a+b)}^{3a+4b} f(y')dy'$$

$$\Phi_4 = \int_{6(a+b)}^{6a+7b} f(y')dy' - \int_{5(a+b)}^{5a+6b} f(y')dy'$$

$$\Phi_5 = \int_{8(a+b)}^{8a+9b} f(y')dy' - \int_{7(a+b)}^{7a+8b} f(y')dy'$$

$$\Phi_6 = \int_{10(a+b)}^{10a+11b} f(y')dy' - \int_{9(a+b)}^{9a+10b} f(y')dy'$$

By similar argument, the magnetic flux produced in area s1 by the kth turn can be written as

$$\Phi_{k+1} = \int_{2k(a+b)}^{2k(a+b)+b} f(y')dy' - \int_{(2k-1)(a+b)}^{2k(a+b)-b} f(y')dy' \qquad (k=1, 2, 3, \cdots\cdots, n) \tag{4-14}$$

Repeating the above steps, we can calculate magnetic flux for a coil of any number of turns. The total magnetic flux in area ABCD of a coil with n turns can be written as

$$\Phi t1 = \Phi_1 + \Phi_2 + \Phi_3 + \Phi_4 + \Phi_5 + \Phi_6 + \cdots\cdots + \Phi_n \tag{4-15}$$

Similarly, the total magnetic flux produced in area A'B'C'D' is

$$\Phi t2 = \Phi_1 + 2\Phi_2 + \Phi_3 + \cdots\cdots + \Phi_{n-1} \tag{4-16}$$

and in area A"B"C"D", the total magnetic flux is

$$\Phi t3 = \Phi_1 + 2\Phi_2 + 2\Phi_3 + \cdots\cdots + \Phi_{n-2} \tag{4-17}$$

etc.. Thus, the total magnetic flux produced in the coil by all coil sections parallel to sections AB and ab can be written as

$$\Phi I = 2(n\,\Phi_1 + \sum_{k=2}^{n} 2(n-k+1)\Phi_k) \tag{4-18}$$

For a coil with 6 turns

$$\Phi I = 2(6\cdot\Phi_1 + 10\cdot\Phi_2 + 8\cdot\Phi_3 + 6\cdot\Phi_4 + 4\cdot\Phi_5 + 2\cdot\Phi_6) \tag{4-19}$$

It is noticed that we have treated the end side of the end turn coil section in the same as that of the sections parallel to it and assumed that the end side of the end turn is divided into two equal parts. In fact , we should replace ℓ with 2ℓ +b in f(y') for the end side coil section in the magnetic flux calculations contributed by that section. However, this should not produce much difference. Therefore, we simply leave it as it is.

By similar analysis, we can obtain the magnetic flux produced in the secondary coil by coil sections AD, A'D', A"D", ad, a'd', a"d", and CB', C'B", cb, and c'b", etc. The

magnetic flux produced by coil sections perpendicular to coil section AB in the central aisle is

$$\Phi II = (n-1)\frac{\mu I}{\pi}\int_0^b \frac{y'.(\sqrt{(2a+b)^2+y'^2+g^2}-\sqrt{y'^2+g^2})}{y'^2+g^2}dy' \tag{4-20}$$

The magnetic flux produced by the side coil sections perpendicular to coil section AB at side edges is

$$\Phi III = n\frac{\mu I}{\pi}\int_0^{2\ell+b} \frac{y'.(\sqrt{b^2+y'^2+g^2}-\sqrt{y'^2+g^2})}{y'^2+g^2}dy' \tag{4-21}$$

for coil sections perpendicular to section AB at turn edges. The total magnetic flux in the coil can now be written as

$$\Phi = \Phi I + \Phi II + \Phi III \tag{4-22}$$

Based on the discussions in this section and equation (4-22), the relationship between magnetic flux and coil gap can be easily proved.

4.2 Magnetic Flux Linkage with the Coil Gap

It has already been shown that the magnetic flux density decreases sharply with the distance from the current carried coil. This suggests that only the nearest turns need to be considered in the magnetic flux calculations. This is true in all of calculations for different coils with different turns. In figure 4.4, the magnetic flux versus coil gaps is shown for a coil with 6 turns. Curve 1 represents the result from full calculation and curve 2 considered only the nearest 2 turns in the magnetic flux calculation, i.e. only Φ_1, Φ_2 and Φ_3 were considered. It is known from the figure that there is negligible difference between the two curves. So it is enough to consider only the nearest two turns in our

calculations. In fact, the calculations for different coils with different turns show similar results. This will let us to consider only the nearest two turns in all magnetic flux calculations.

Figure 4.5 shows the magnetic flux versus coil gaps for different coils with different turns. As the turns increase, the magnetic flux increases. This can be easily understood because the increase in turns means the increase in coil area and coil length. More magnetic flux will be produced in the secondary coil plane. The increase in turns also means the increase in diaphragm area.

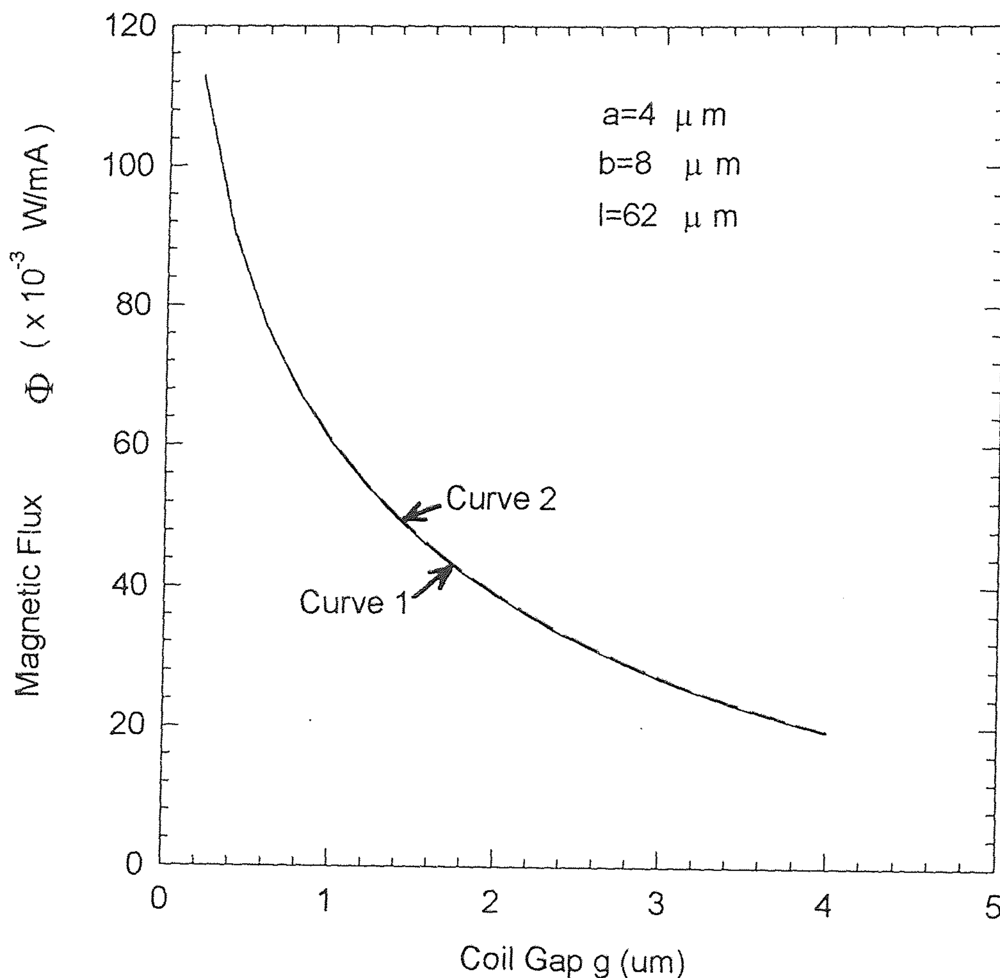

Figure 4.4 Magnetic flux versus mechanical gaps for a coil with 6 turns. Curve 1 is from the full calculations including all turns and curve 2 represents the results with only two nearest turns considered in the calculations

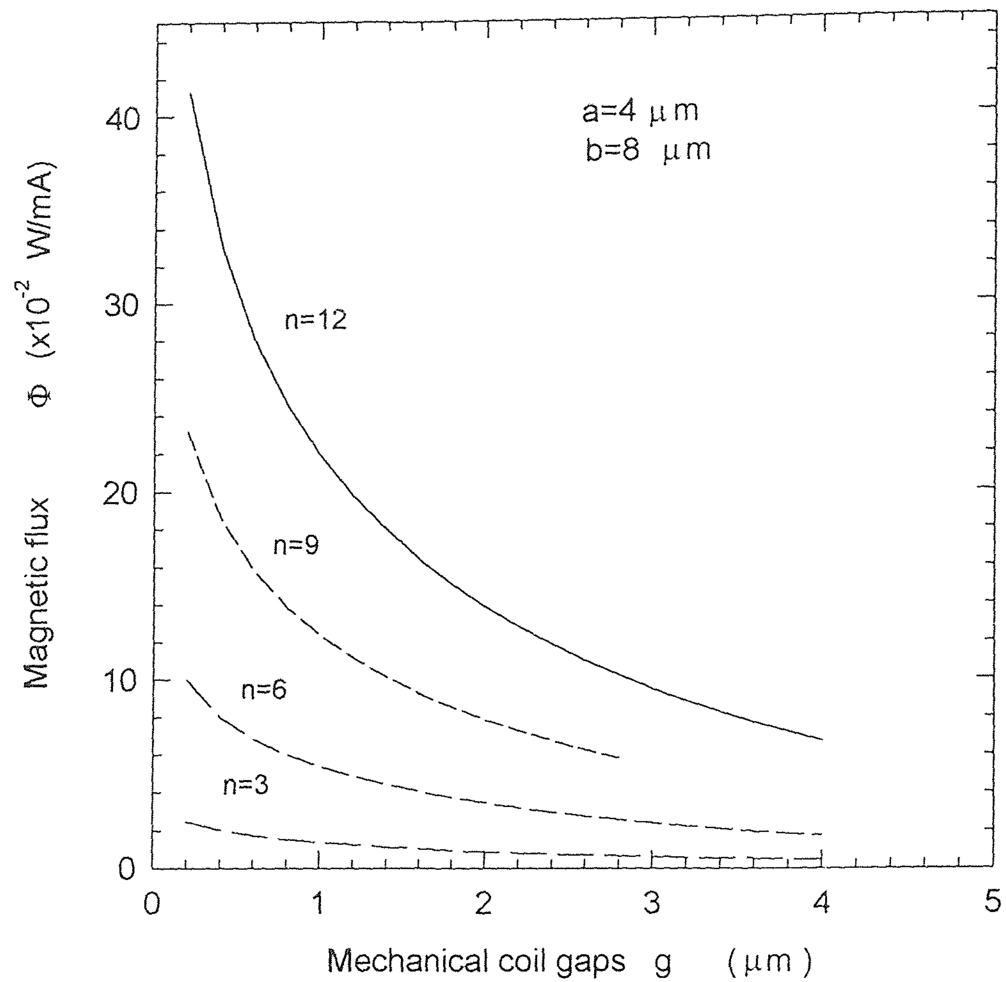

Figure 4.5 Magnetic flux versus mechanical coil gaps for different coils with different turns

4.3 Voltage Output Vo Calculation

The output voltage Vo in the secondary coil, by definition, is the differentiation of the magnetic flux with respect to time. This is obtained by differentiating the both sides of equation 4-22. This is expressed as

$$V_o = \frac{d\Phi}{dt} \tag{4-23}$$

$$= \omega I_o \cos(\omega t) E(g) \tag{4-24}$$

where

$$E(g) = 2n\int_0^b \frac{y'(\sqrt{\ell^2 + y'^2 + g^2} - \sqrt{y'^2 + g^2})}{y'^2 + g^2} dy'$$

$$+\sum_{k=2}^{n} 2(n-k+1)(\int_{2k(a+b)}^{2k(a+b)+b} \frac{y'(\sqrt{\ell^2 + y'^2 + g^2} - \sqrt{y'^2 + g^2})}{y'^2 + g^2} dy'$$

$$-\int_{(2k-1)(a+b)}^{2k(a+b)-b} \frac{y'(\sqrt{\ell^2 + y'^2 + g^2} - \sqrt{y'^2 + g^2})}{y'^2 + g^2} dy')$$

$$+(n-1)\int_0^b \frac{y'(\sqrt{(2a+b)^2 + y'^2 + g^2} - \sqrt{y'^2 + g^2})}{y'^2 + g^2} dy'$$

$$+n\int_0^{2\ell+b} \frac{y'(\sqrt{b^2 + y'^2 + g^2} - \sqrt{y'^2 + g^2})}{y'^2 + g^2} dy'$$

Figure 4.6 shows the output voltage as a function of coil gaps. Following parameters are used in the calculations:

f=200 MHz

Io=100 mA

Although single level coils are used for calculation, the results shown here are consistant with that obtained from double level coils by Okojie[34].

As the magnetic flux Φ depends on the coil parameters, so does the output voltage Vo. It is also apparent that the output voltage depends on the frequency and the amplitude of the applied current in the primary coil. The above calculations assumed a finite length coil. By choosing the frequency and the amplitude of the applied current and coil parameters, a specific output in the secondary coil can be obtained. Equation 4-24 lays the guideline for the design of a specific magnetic coupled high temperature pressure sensor.

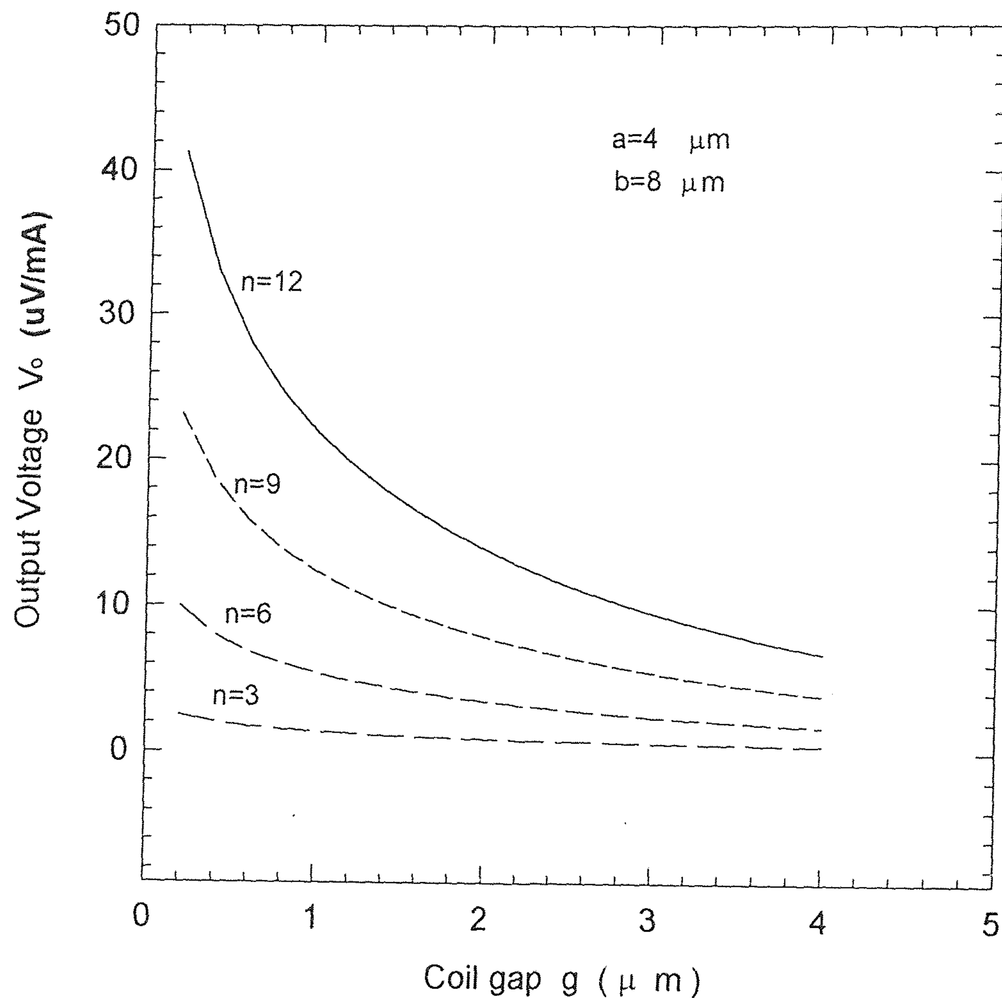

Figure 4.6 Voltage output Vo as a function of coil gap g for different coils with different turns

CHAPTER 5

MECHANICAL DESIGN OF THE SENSOR DEVICE

5.1 Overview

For micromechanical applications, a material should satisfy some basic requirements: 1) its Young's modulus should be reasonably high so that it can retain its elasticity and has little hysteresis in responding an applied load within a certain load range, 2) the definition and micromachining of the device shapes and patterns should be controllable in a easy way, 3) preferably, the techniques for device production as a whole should be capable of high precision and be amenable to miniaturization.

It has already been shown that silicon could fulfill the above mentioned requirements. Used as a mechanical material, silicon was thoroughly reviewed by K. Peterson[1] in 1982. In the past decade, silicon played a crucial role and many successful applications in micromechanical device development has been demonstrated. Firstly, there is a well established technology for silicon microelectronics, and secondly, this same technology can equally be exploited in the design and manufacture of a wide spectrum of miniature mechanical devices and components. There are a variety of reports of successful stories about the micromechanical devices realized by silicon microfabrication[14-18]. Therefore, silicon is also chosen in this thesis as the basic material for the high temperature pressure sensor. In order to use silicon, p-n juctions have been eliminated from the design.

5.2 Deflection of a Loaded Thin Square Diaphragm

It is well established by S. P. Timoshenko that the center deflection of a clamped thin square diaphragm under a uniform load (such as pressure) is expressed by the equation below[19]

$$y = \frac{\alpha P d^4}{E h^3} \tag{5-1}$$

where

α=0.0138

P= applied pressure on the diaphragm

d=side length of the loaded thin square diaphragm

E=Young's modulus

h=diaphragm thickness

Equation 5-1 governs the small deflection of a square thin diaphragm. This means that the maximum deflection of the diaphragm is less the thickness of the diaphragm. Figure 5.1 shows the deflection of a thin diaphragm versus the applied pressure. There is a linear response of the diaphragm deflection to the applied pressure, as is evidently predicted by Equation 5-1.

Equation 5-1 established the critical standard in the design of thin square diaphragm pressure sensors. It determines that the maximum pressure can be applied onto the diaphragm to get a linear response. If, however, a large diaphragm deflection is expected, i.e. the maximum deflection of the diaphragm is larger than the thickness of the diaphragm, a different equation should be used instead of equation 5-1[18]. This case will not be discussed further here and only the small deflection is considered in this thesis.

5.3 Mechanical Gap as a Function of Fluid Pressure

In this section, we will establish the relationship between the mechanical gap and the applied pressure. When a pressure is applied onto a diaphragm, the diaphragm will deflect as it has been discussed in the previous section. If the original coil gap is g_o when there is no pressure applied on the diaphragm, the gap will change to g when pressure is applied onto the diaphragm according to the following equation:

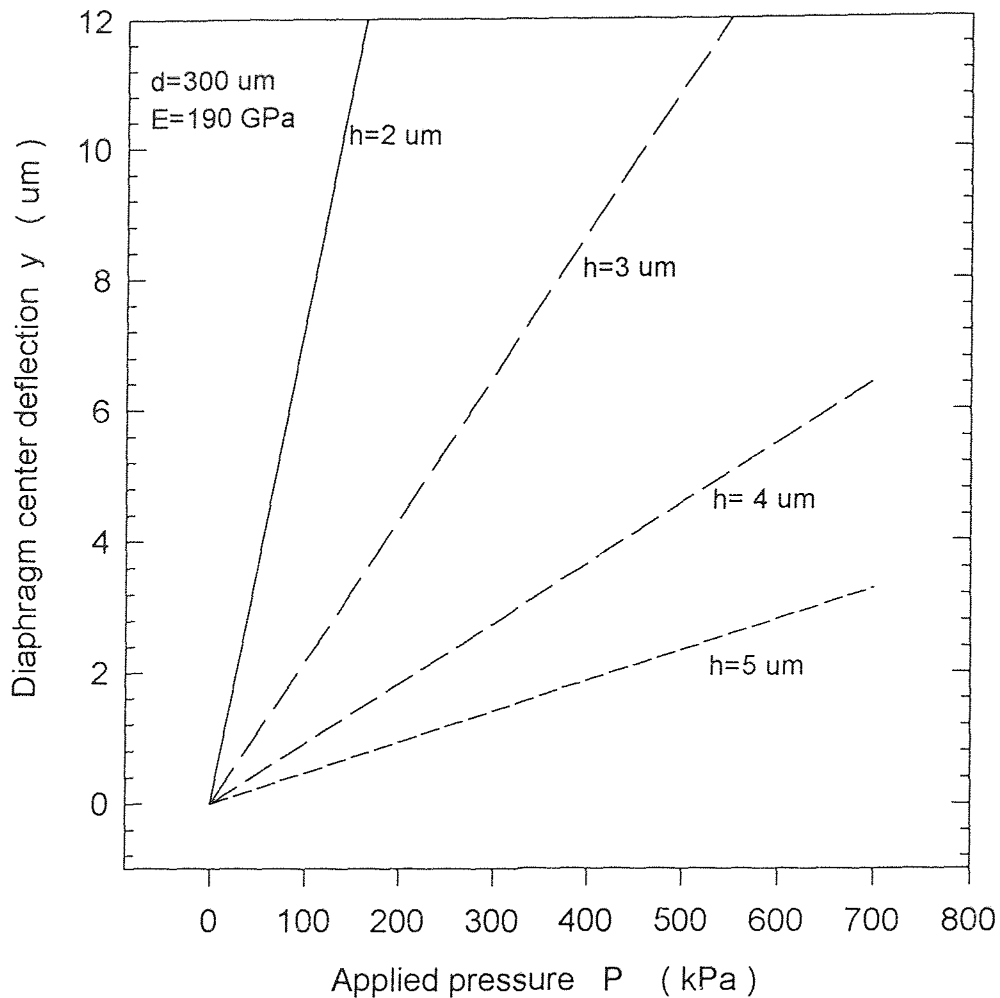

Figure 5.1 Diaphragm center deflection y as a function of applied pressure for a square diaphragm of side length d=300 μm and with different diaphragm thickness h as a parameter

$$g = g_o - y \tag{5-2}$$

$$= g_o - \frac{\alpha P d^4}{E h^3} \tag{5-3}$$

Figure 5.2 plots out the coil gap versus the differential pressure for a certain diaphragm thickness. The coil gap g deflects linearly with the applied pressure P, which is predicted by equation 5-3. If an applied pressure reaches a value such that the deflection

of the diaphragm equals original coil gap g_o, the coil gap becomes zero. This means that the diaphragm has deflected to its limit, to the ' touching ' the primary coil. The applied pressure at this point is the maximum pressure that can be measured using this sensor. Larger pressures over 400 kPa in using a sensor with diaphragm size of 300μm × 300 μm are overrange.

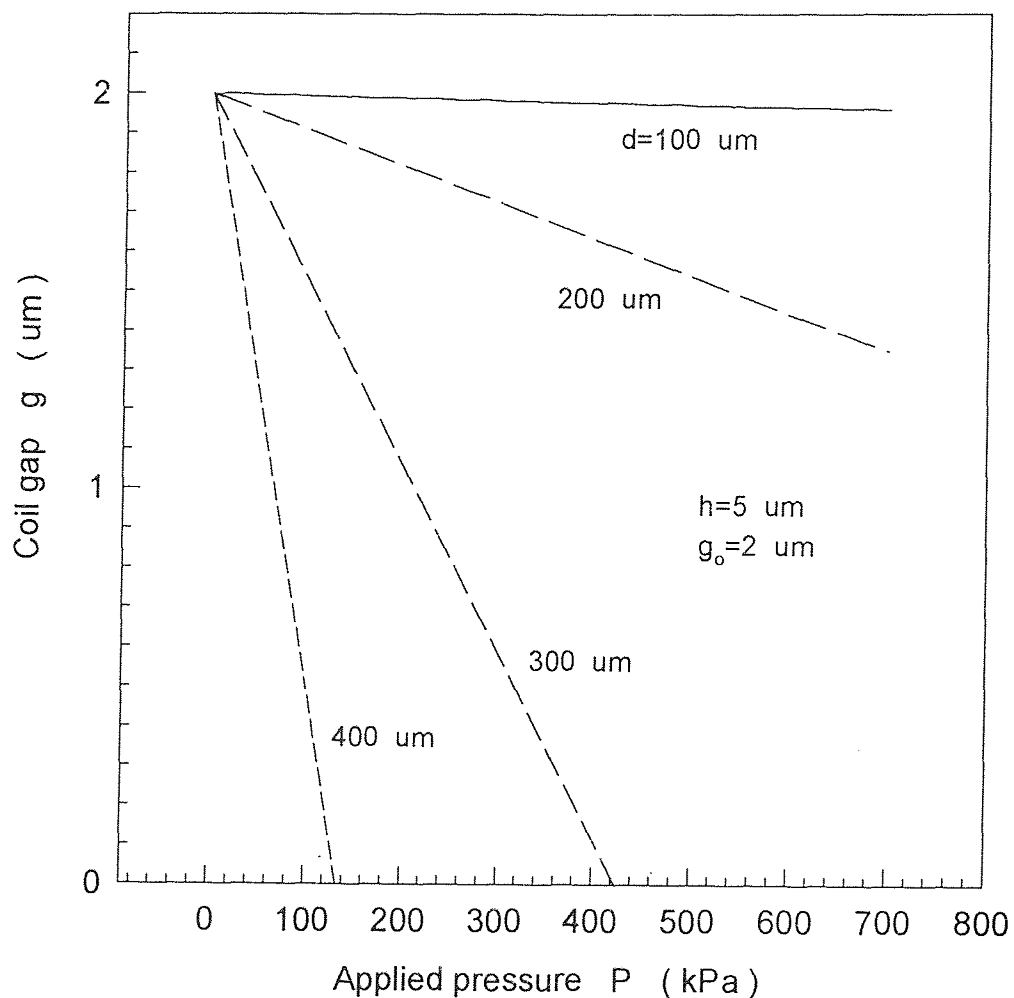

Figure 5.2 Coil center gap g versus applied pressure P for different sized thin diaphragms but with the same diaphragm thickness h

CHAPTER 6

SENSOR DEVICE DESIGN

The previous two chapters establish the basic principles for the sensor operation. This chapter will discuss the device design based on the established principles and equations in the previous two chapters. We will discuss the following issues: 1) output voltage as a function of fluid pressure, 2) pressure sensitivity, 3) output voltage as a function of coil parameters-turns n and pitches, and 4) temperature effects on device performances.

6.1 Output Voltage as a Function of Fluid Pressure

In this section, we will discuss the output voltage as a function of fluid pressure and other issues such as response linearity and pressure sensitivity. These issues are important to the device operation. They determine what useful range of the pressure can de measured and what accuracy the device is. In all, they determine the usability of a sensing device. Again only the transfer function calculation for small diaphragm deflection is considered in this chapter.

6.1.1 Voltage Response to Fluid Pressure

The transfer properties of a device is utmost essential to the usefulness of the device. In fact, what the transfer function calculation is that it essentially evaluates the induced output voltage Vo in the secondary coil by flowing an alternative current through the primary coil while pressure is uniformly applied on the diaphragm. In this regard, equation 4-24 is related to coil gap and therefore to applied pressure through equation 5-3. For the sake of convenience, the output voltage equation is reintroduced here:

$$V_o(P) = \frac{\mu}{\pi}\omega I_o \cos(\omega t) E(P) \qquad (6\text{-}1)$$

where

$$E(P) = 2n\int_0^b \frac{y'(\sqrt{\ell^2 + y'^2 + g^2} - \sqrt{y'^2 + g^2})}{y'^2 + g^2} dy'$$

$$+\sum_{k=2}^{n} 2(n-k+1)\left(\int_{2k(a+b)}^{2k(a+b)+b} \frac{y'(\sqrt{\ell^2 + y'^2 + g^2} - \sqrt{y'^2 + g^2})}{y'^2 + g^2} dy'\right.$$

$$\left. - \int_{(2k-1)(a+b)}^{2k(a+b)-b} \frac{y'(\sqrt{\ell^2 + y'^2 + g^2} - \sqrt{y'^2 + g^2})}{y'^2 + g^2} dy'\right)$$

$$+(n-1)\int_0^b \frac{y'(\sqrt{(2a+b)^2 + y'^2 + g^2} - \sqrt{y'^2 + g^2})}{y'^2 + g^2} dy'$$

$$+n\int_0^{2\ell+b} \frac{y'(\sqrt{b^2 + y'^2 + g^2} - \sqrt{y'^2 + g^2})}{y'^2 + g^2} dy' \qquad (6\text{-}2)$$

and

$$g = g_0 - \frac{\alpha P d^4}{E h^3} \qquad (6\text{-}3)$$

Now the output voltage is expressed as a function of applied pressure. From this equation and equation 5-3, it is possible to analyze the response of the sensor output voltage to the applied pressure. We should recall that there is no explicit analytical expression for the output voltage. The applied pressure has to be substituted into equation 6-2 through equation 6-3 to get the output voltage Vo(P) from equation 6-1.

If the original coil gap g_0 is chosen to be 2 μm, then the maximum applied pressure is determined by equation 6-3 such that g =0. If the applied pressure is higher than the applied pressure, the output voltage becomes seriously nonlinear, and incorrect results will be given out. This case should be avoided. On the other hand, the applied pressure should also large enough so that the output voltage should not fall into the noise level. This sets up the useful range that the sensor can be applied.

Now, we come to the point to determine the response of the output voltage Vo(P) to the applied pressure. In this regard, the side length d, thickness h, and Young's modulus E are chosen at the fixed value. With the diaphragm side length d=300 μm, thickness h=5 μm, coil turns n=9, and Young's modulus of the diaphragm material (Si) E=190 GPa, the output voltage as a function of the applied pressure is plotted out in figure 6.1. For the current frequency f=200 MHz and the current magnitude Io=100mA, the maximum output voltage induced in the secondary coil is 272 mV at the applied pressure P= 400, at which the diaphragm deflection is 2 μm, equal to the original coil gap. While at zero applied pressure differential, the output voltage(offset voltage) is 78 mV. The dynamic output range is 194 mV.

We see that an overrange condition will result if we want this device to measure the pressures larger than 400 KPa. This pressure is the maximum pressure the sensor can be used to measure. At this point, the magnetic flux almost fully passes through the secondary coil plane and the diaphragm has deflected to nearly touch the primary coil.

Further increase in applying pressure will not increase the magnetic flux through the secondary coil plane. Therefore, there is no increase in output voltage in response to the applied pressure. This is shown in the figure 6.1 as almost a flattened output curve near the maximum pressure(400 KPa).

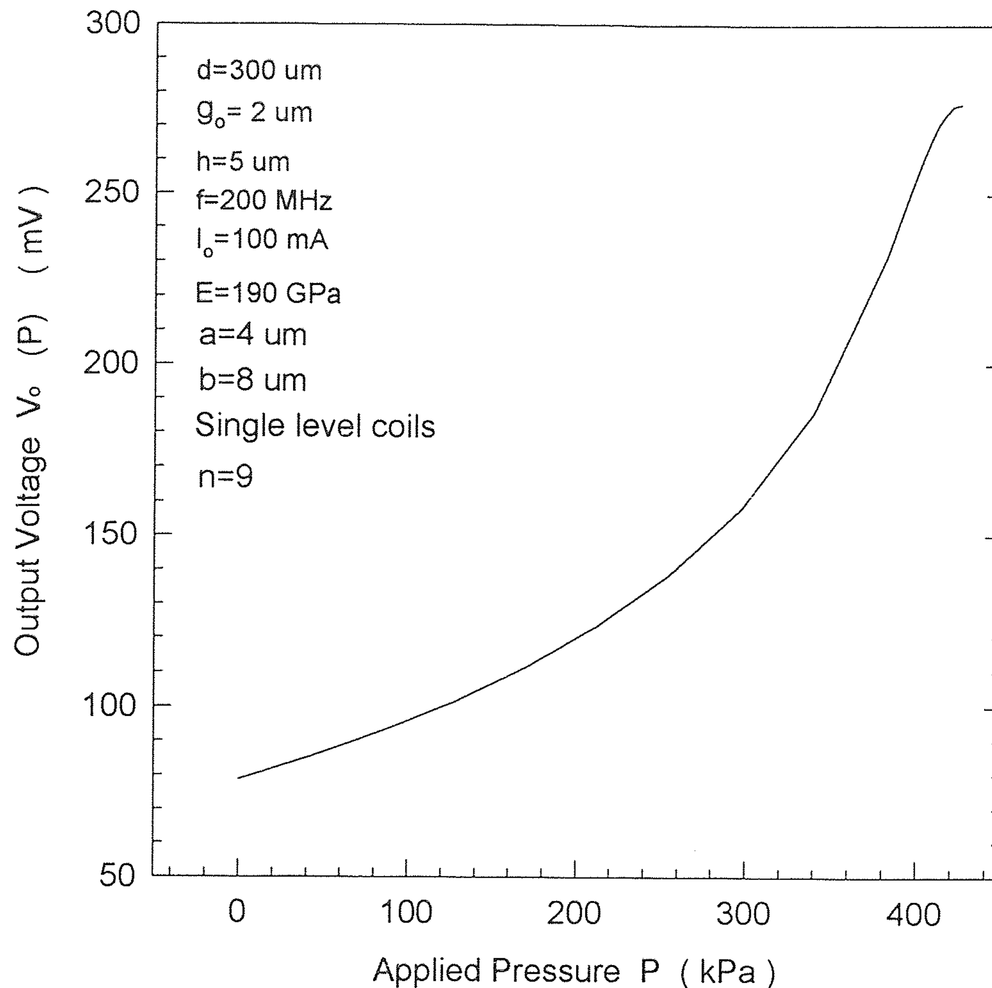

Figure 6.1 Output voltage as a function of applied pressure for MCHTPS with the diaphragm area =300 ×300 μm^2 and thickness h=5 μm

6.1.2 Device Response Linearity

The response linearity determines what the accuracy of a device is, and what the measures such as circuitry compensation have to be taken to make the device accurate and applicable. In practical devices, we hope to get a linear output voltage in response to the input signal(applied pressure in our case). The more linear the response, the less the circuitry compensation is required. However, all the physical properties of the material are

generally not linearly related to outside factor variations, the response of the output voltage to applied pressure is also not expected to be linear. This is clearly observed in figure 6.2. For commonly used pn-junction-based piezoresistive type pressure sensors, there are generally much more linear response characteristics than that of magnetic coupled inductive pressure sensors described in this thesis. However, the former can not operated at temperatures high than 150 °C, the later can work at temperatures up to 600° C. There is a trade-off between a linear response and high temperature operation. In figure 6.2, the calculated response is compared with a best fitted straight line response. This output characteristics suggest that different approach for circuit conditioning from that for piezoresistive type pressure sensor has to be taken in practical applications.

6.1.3 Output Voltage Sensitivity to Applied Pressure

Output voltage sensitivity to the applied pressure is another important factor in evaluating the sensor device characteristics. The analysis of this issue is done by taking the derivative of the output voltage expressed in equation 6-1 with respect to pressure. The output voltage is related to pressure through the diaphragm deflection. Therefore, by differentiating the output voltage with respect to pressure, we obtain the response sensitivity as

$$\frac{dV_o}{dP} = \frac{dV_o}{dg} \cdot \frac{dg}{dP} \tag{6-4}$$

According to equation 6-3

$$\frac{dg}{dP} = -\frac{\alpha d^4}{Eh^3} \tag{6-5}$$

$$\frac{dV_o}{dg} = \frac{\omega \mu I_o \cos(\omega t)}{\pi} \cdot \frac{dE(P)}{dg} \tag{6-6}$$

Therefore

$$\frac{dV_o}{dP} = -\frac{\alpha d^4}{Eh^3} \cdot \frac{\omega\mu I_o \cos(\omega t)}{\pi} \cdot \frac{dE(P)}{dg} \tag{6-7}$$

where

$$\frac{dE(P)}{dg} = 2ng\int_0^b \left(\frac{y'}{y'^2+g^2} - \frac{y'(2\ell^2+y'^2+g^2)}{(y'^2+g^2)^2\sqrt{\ell^2+y'^2+g^2}}\right)dy'$$

$$+g\sum_{k=2}^{n} 2(n-k+1)\left\{\int_{2k(a+b)}^{2k(a+b)+b} \left(\frac{y'}{(y'^2+g^2)^{3/2}} - \frac{y'(2\ell^2+y'^2+g^2)}{(y'^2+g^2)^2\sqrt{\ell^2+y'^2+g^2}}\right)dy'\right.$$

$$\left. -\int_{(2k-1)(a+b)}^{2k(a+b)-b} \left(\frac{y'}{(y'^2+g^2)^{3/2}} - \frac{y'(2\ell^2+y'^2+g^2)}{(y'^2+g^2)^2\sqrt{\ell^2+y'^2+g^2}}\right)dy'\right\}$$

$$+(n-1)g\int_0^b \left(\frac{y'}{(y'^2+g^2)^{3/2}} - \frac{y'((2a+b)^2+y'^2+g^2)}{(y'^2+g^2)^2\sqrt{(2a+b)^2+y'^2+g^2}}\right)dy'$$

$$+ng\int_0^{2\ell+b} \left(\frac{y'}{(y'^2+g^2)^{3/2}} - \frac{y'((2b^2+y'^2+g^2)}{(y'^2+g^2)^2\sqrt{(b^2+y'^2+g^2}}\right)dy' \tag{6-8}$$

Again, the integration 6-8 can only be done in numerical way. Based on equations 6-7 and 6-8, the output voltage sensitivity for a coil of 9 turns is shown in figure 6.3. For a coil of 9 turns, the output voltage sensitivity to the applied pressure is low at small applied pressures and increases slowly with the applied pressure at the beginning. The output voltage sensitivity begins to increase sharply at about 350 kPa, which corresponds to the

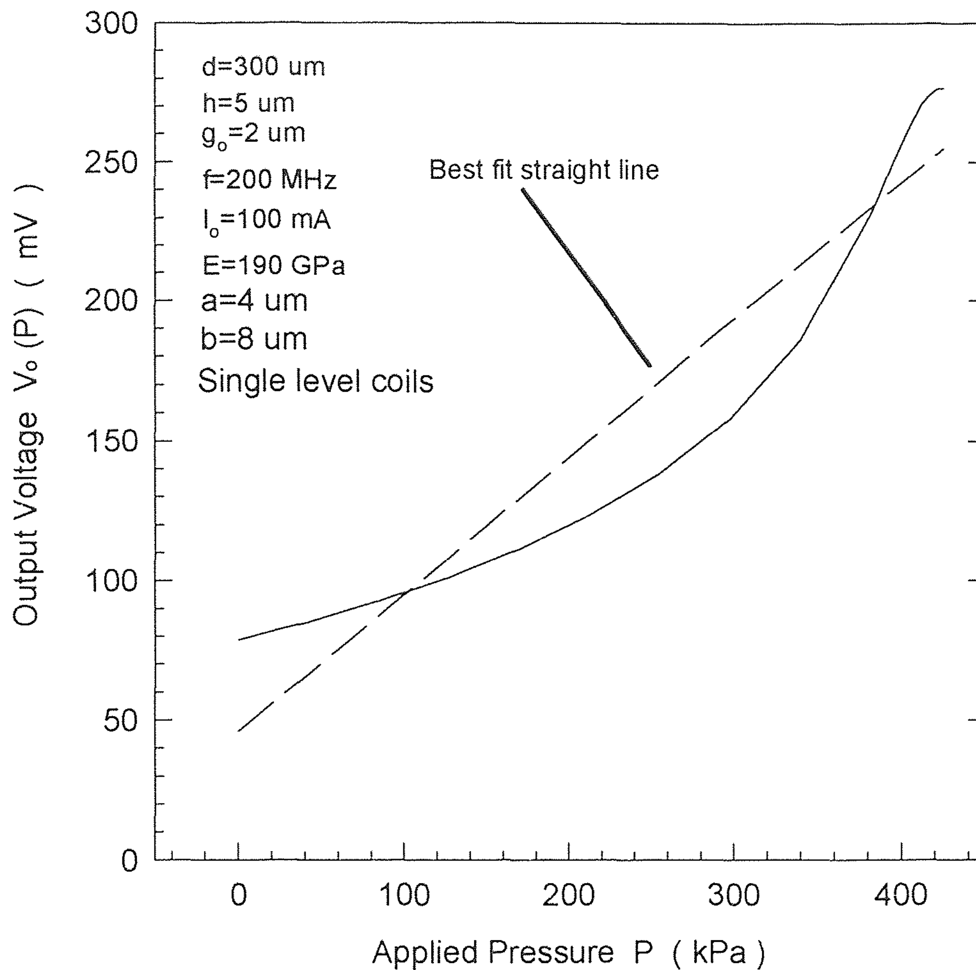

Figure. 6.2 The linearity of the output voltage to applied pressure differential

coil gap g=0.3 μm. This is coincided with the results from figure 6.1. This can be understood as follows: when the applied pressure is low, the diaphragm deflection is small and the magnetic flux through the secondary coil is small because the two coils are far apart. The induced voltage in the secondary coil is also small. When the applied

pressure is large enough such that the two coils come closer, the magnetic flux in the secondary coil plane becomes high, the induced voltage in the secondary coil also becomes large. However, the sensitivity decreases quickly to almost zero after experiencing a maximum, which corresponding to a diaphragm deflection close to the limit value. Once again, it shows that the voltage sensitivity is non-linear.

6.1.4 The Effects of Coil Turns and Coil Pitches on the Output Voltage

Device parameters affect the output performance. We have already shown in chapter 4 that the output voltage depends greatly on the coil turns and therefore on the diaphragm dimensions. Figure 6.4 plots out the output voltage versus the applied pressure differential for different coil turns for a original coil gap of 2 μm. It can be seen that more turns lead to higher output voltage. It is clearly indicated in the figure that moderate number of turns must be designed to obtain a reasonable output. But if the turn number is fewer than 9, the output is low. A coil of 9 or more turns will lead to reasonably high output. The number of turns reflects the dimension of diaphragms. More turns generally means larger diaphragms. This should be taken into consideration in the design of a specific MCHTPS. In our discussions, A coil of 9 turns is generally referred.

Coil pitches also affect the output voltages. Figure 6.5 shows the output voltage versus applied pressure coils of 9 turns but with different coil pitches: one with coil line width of 2 μm pitch of 10 μm, the other with coil line width of 4 μm and pitch of 8 μm. We could not see much difference in output voltage for these two devices. However, this does not necessarily mean that the line width and coil pitch do not affect the output

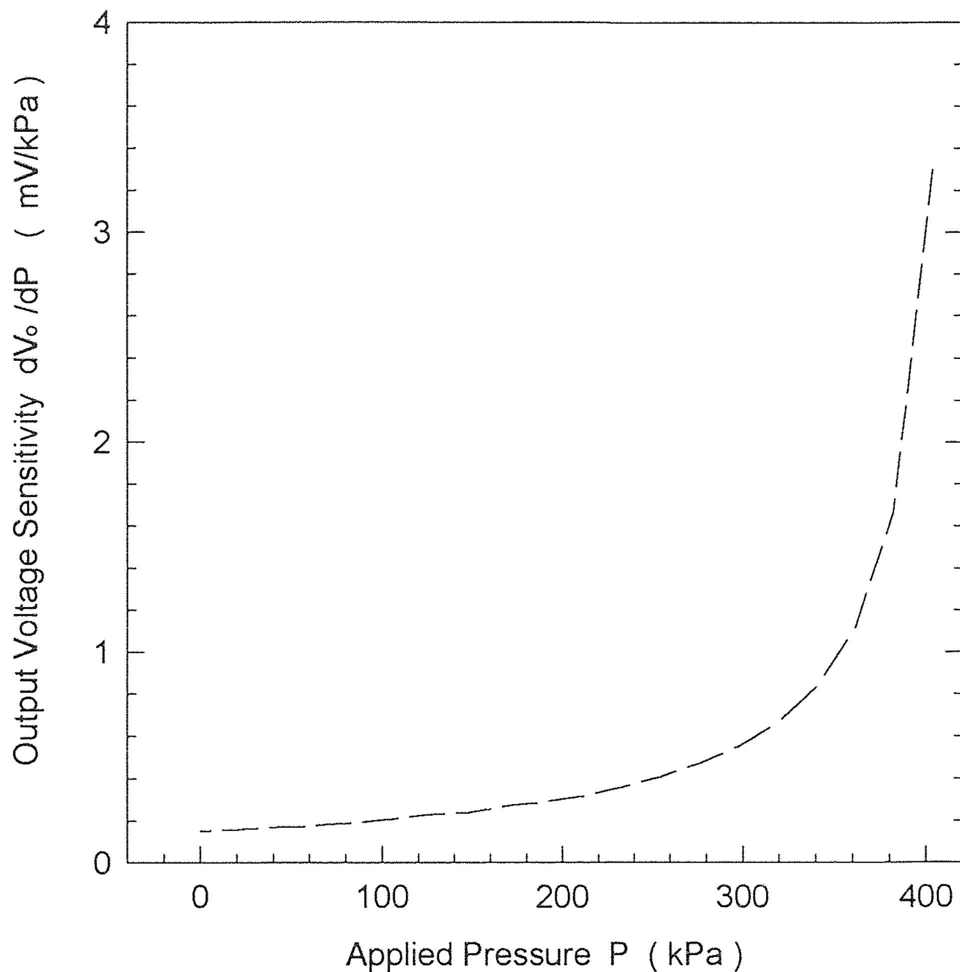

Figure 6.3 Output voltage sensitivity as a function of applied pressure for a sensor device of diaphragm area=300×300 μm^2 , thickness h=5 μm and original coil gap g_0 =2 μm

voltages.As the coil pitch goes down to the value close to the coil gap, difference would occur. This could be understood from figure 4.3. If the coil pitch is close to or less than the coil gap, the magnetic flux contributed from the adjacent turns may become significant. This is a destructive component. This component is undesirable and should be avoided. The problems would also occur in the device fabrication if the coil pitch is too small because any misalignment between the two coils will translate into decrease of magnetic

flux and therefore the output voltage in the secondary coil. However, the requirement for coils alignment is not so stringent for the large coil pitches due to the fact that the magnetic flux density decreases quickly with the distance away from the current-carried coil and the magnetic flux contribution from the adjacent coil becomes small. So the design should include the considerations of these factors.

The thing is that the large coil pitches and coil turns require a large diaphragm. There is a trade-off between device dimensions and coil turn number requirements. The specific application requirement asks for specific design considerations.

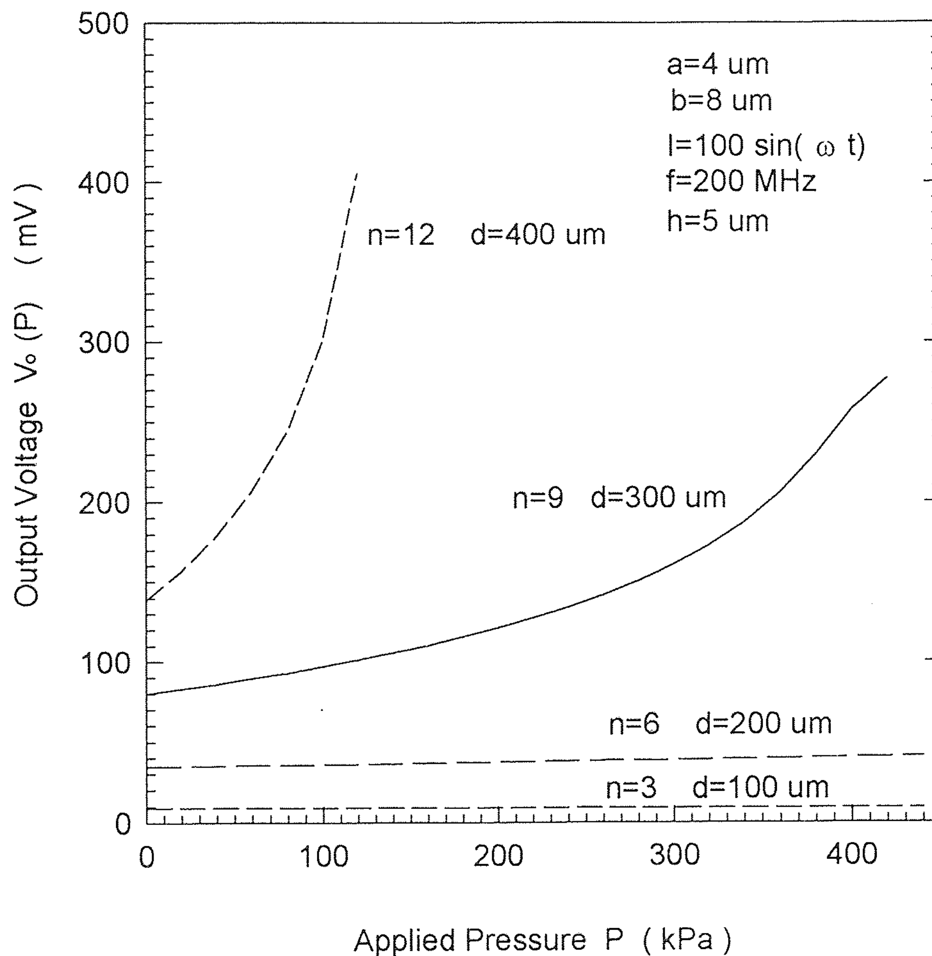

Figure 6.4 Output voltage versus applied pressure differential for different coil turns

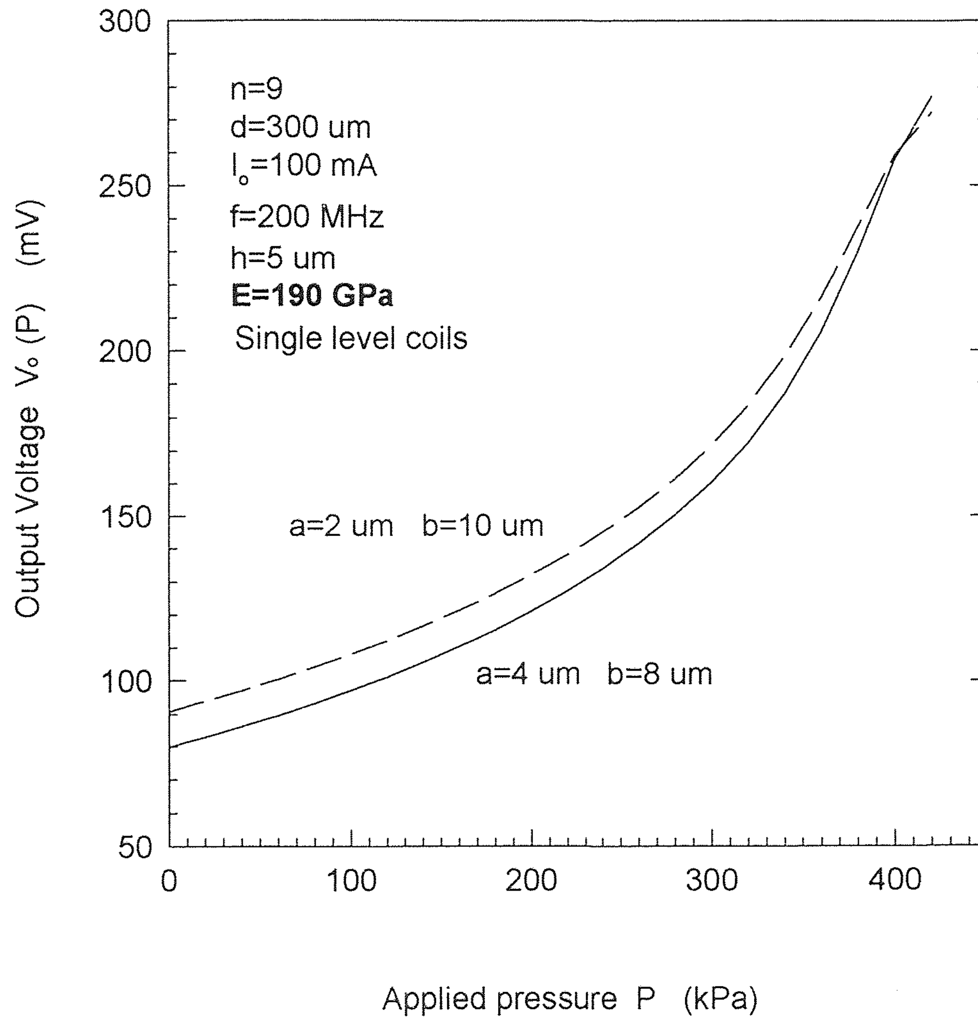

Figure 6.5 Output voltage versus pressure for devices with different coil pitches

6.2 Temperature Effects on the Sensor Performance

There is virtually no physical property independent of temperature. Any properties of a material is temperature sensitive and this temperature dependence could affect the interpretation of the measured results. Temperature sensitivity of a thin film material usually results thermal stress in the films. For micromechanical devices, thermal stress causes changes of device characteristics with temperature. This will results in reliability problem. For high temperature applications, the temperature effects on the sensor performance is especially important. The main issue of our discussion in this section is that of the thermal stress, its effects on the output properties.

6.2.1 Temperature Effects on the Stress of the Diaphragm

Thermal stress exists in almost all composite layered structures. The main source of this stress comes from the mismatch of the thermal expansion properties of different materials. There are two types of stresses: one is compressive and the other is tensile. Figure 6.6a [20] shows schematically the tensile stress in which the film on the substrate tends to expand. However, the compressive stress shown in the figure 6.6b indicates that the film on the substrate tends to constrict.

Thermal stress has a profound effects on the device performance, especially at elevated temperatures. It directly affects the applicability and survivability of a device at high temperatures in one way or another. At high temperatures, thermal mismatch between layers and other components become more pronounced due to different thermal coefficients of expansion(TCE). The usual consequence is the short life span and subsequent failure of the device.

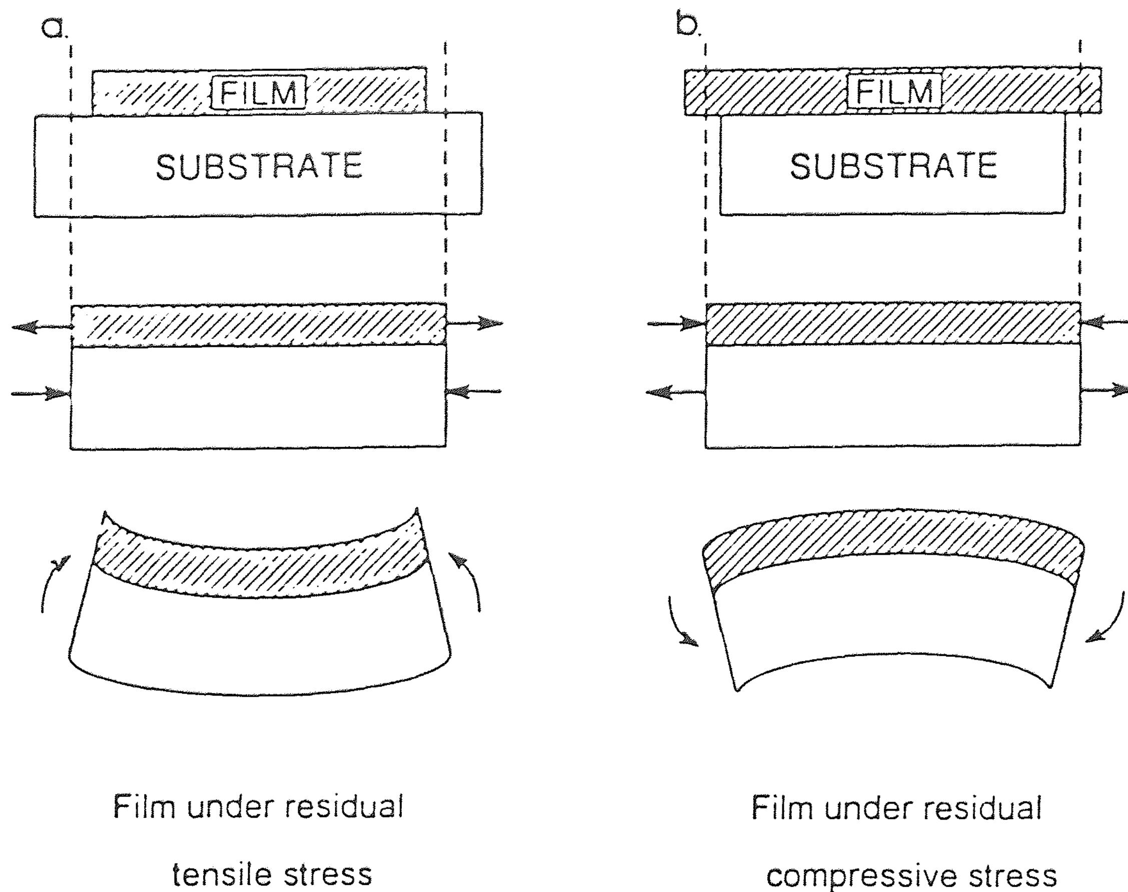

Figure 6.6. Sequence of events leading to (a) residual tensile stress in film; (b) residual compressive stress in film

For the existing piezoresistive type pressure sensors, thermal effects have even larger effects on their performance because of the high temperature coefficient of resistance(TCR). Normally, external circuitry is usually adopted for temperature compensation[21]. However, at very high temperatures above, for example, 400 °C, circuitry compensation can become impractically troublesome. As the thermal effects are usually intrinsic to any devices, the better way to reduce such thermal effects is to better

design the device structure that would require minimum external circuit conditioning at high temperatures.

The pressure sensor described in this thesis adopts a unique structure design and uses the unique properties of metal silicides, such as tatanlum silicide ($TaSi_2$) and platinum silicide (PtSi). Table 6.1 lists some properties of some silicides and high temperature metals normally encountered in VLSI development[22,23]. It can be seen from the table 6.1 that many choices can be made for coil materials from those listed in the table. However, considerations have to be taken for the device realization in device manufacture in addition to the matching the layer properties at elevated temperatures. In this regard, platinum or platinum silicide can be selected. Firstly, both Pt and PtSi have low resistivity(30 μΩ-cm for PtSi and 10.6 μΩ-cm for Pt) and this makes them viable as the interconnect for low power dissipation devices. Secondly, both materials have high melting point above 1400°C, and this would make them stable and applicable for high temperature operation above 600°C. Lastly, direct wire bonding can be made on them without double deposition of metal films for out-connect wire bonding. Wire-bondable material is needed if other material is used as coil material. For most micromachined devices, post-micromachining deposition of contact materials and then applying photolithography is usually undesirable and sometimes impractical and should be avoided, which will be discussed later in chapter 7.

The thermal stress $\sigma_{t,th}$ between film and substrate is given by[24]

$$\sigma_{t,th} = \frac{E_f}{1-\nu_s}\int(\alpha_s(T)-\alpha_f(T))dT \qquad (6\text{-}9)$$

where E, α, and ν are Young's Modulus, thermal expansion coefficient and poison's ratio, respectively. The subscripts f and s refer the film and substrate respectively. The integration goes from ambient temperature T_0 to final temperature T. Because the substrate thickness is much larger than the oxide and coil metal thickness, the thermal

Table 6.1 Relevant properties of silicides and high temperature metals compared with silicon at 25 °C

Material	Resistivity μΩ-cm	Temperature Coefficient of Expansion ppm/K	Melting Point °C	Young's Modulus GPa
$TiSi_2$ (Co-sputtered) (Metal/poly-Si)	25 13-16	12.5	1540	
$TaSi_2$ (Co-sputtered) (Metal/poly-Si)	50-55 35-45	8.8, 10.7	2400	
$MoSi_2$ (Co-sputtered)	100	8.75	1870	
WSi_2 (Co-sputtered)	70	6.25, 7.90	2050	
$NiSi_2$	50-60	12.06		
Pd_2Si (Metal/poly-Si)	30-35			
$PtSi_2$ (Metal/poly-Si)	28-35			
Pt	10.6	9.0	1774	
W	5.5	4.5	3415	410
Ni	6.8	13.3	1455	
Cr	20	6.3	1900	
Mo	5.2	5.0	2625	343
Pa	10.8	11.0	1552	
Si		2.44	1420	190
Pyrex 7740		3.2	1050	

stress is largely determined by the substrate and the glass layer. Assuming constant thermal expansion coefficients, then the equation 6-9 can be rewritten as

$$\sigma_{t,th} = \frac{E_f}{1-\nu_s}(\alpha_s(T) - \alpha_f(T))\Delta T \tag{6-10}$$

The thickness of silicon dioxide is 4000 $\mathring{A}$, and the thickness of the coil metal film is 1000 $\mathring{A}$, much thinner than the silicon diaphragm, 5 μm, the thermal stress is mainly determined by silicon diaphragm and the glass layer(1 μm). In fact, silicon/silicon dioxide interface is quite thermal stable, which has long been proven in the microelectronics development.

The glass used for our device is Pyrex from corning (glass code is 7740). It has thermal expansion of coefficient fairly close to that of silicon from room temperature to 500°C. Table 6.2 lists the thermal expansions of silicon and Pyrex in temperature range from -25 °C to 500°C[29]. This suggests that glass/silicon dioxide interface would have similar thermal behavior to silicon/silicon oxide interface. Therefore, it let us assume that the thermal stress is dominated by silicon substrate and Pyrex glass layer.

We can roughly estimate the thermal stress between the substrate and the film. Assuming the worst case with the mismatch of thermal expansion of coefficient listed in table 6.2 between -25°C and 500°C, E_f =190GPa, equal to that of silicon, $\nu_s = 0.3$, the thermal stress $\sigma_{t,th}$ =5.7 MPa at 100°C and $\sigma_{t,th}$ =44 MPa at 500°C, respectively. These stresses are significant compared with mechanical stress in the diaphragm due to applied pressure onto the diaphragm at lower pressures. However, the general tendency is that the stress is released in some extent at higher temperatures. The above figures might have overestimated the thermal stress effects.

The mechanical stress itself is also affected by temperature. The mechanical stress at the center of a square diaphragm is expressed by[19]

$$\sigma = \frac{0.138Pd^2}{h^2} \tag{6-11}$$

where P is the applied pressure differential, d and h are side length and thickness of the diaphragm, respectively. This stress is temperature dependent because the side length d is temperature dependent. d is related to temperature according to equation

Table 6.2 Thermal expansion characteristics of silicon and 7740 Pyrex glass

Temperature °C	Thermal expansion coefficient of silicon α_{si} (ppm/° C)	Thermal expansion coefficient of Pyrex α_{glass} (ppm/° C)
-25	1.92	3.04
0	2.2	3.2
25	2.48	3.2
50	2.72	3.2
100	2.98	3.26
150	3.28	3.26
200	3.5	3.3
250	3.66	3.28
300	3.78	3.3
350	3.86	3.32
400	3.96	3.32
450	4.02	3.32
500	4.1	4.44

$$d(T)=300(1+\alpha\Delta T) \qquad (\mu m)$$
$$=300(1+2.6\times10^{-6}(T-25)) \qquad (\mu m) \qquad (6\text{-}12)$$

The thickness of the diaphragm can be assumed to have negligible dependence on temperature. With equations 6-11 and 6-12, it is easily seen how much the film stress is dependent upon temperature. The results are depicted in figure 6.7.

It is seen that the temperature effect on the mechanical stress within small deflection range is negligible even up to 500°C. This also reflects that pressure sensors based on

silicon as a mechanical membrane can be safely operated at temperatures up to 500°C or even higher temperatures without loosing much of its mechanical properties.

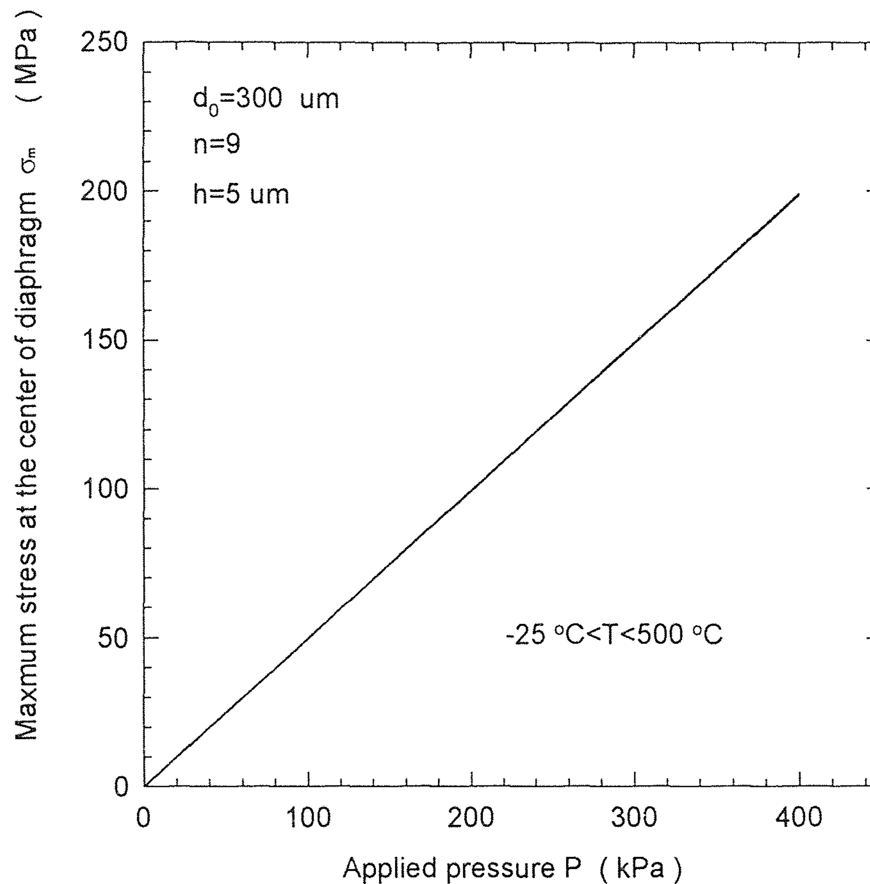

Figure 6.7. Center stress of the diaphragm versus applied pressure at temperatures from -25°C to 500 °C. Note that this plot is independent of Young's modulus which is temperature sensitive

6.2.2 Temperature Effects on Output Voltage

The temperature effect on output voltage comes from different sources. The quantitative calculation of it is not simple because these different sources are generally interrelated to affect the diaphragm and then the output voltage. One source is the mismatch of thermal

expansion of coefficients between different materials that form the diaphragm, or called thermal mismatch. As is already described in the above section, the thermal mismatch should not have significant affect on the output voltage. Another obvious source is reflected from the diaphragm deflection, as depicted by equation 5-3 and recalled below for explicity

$$g = g_0 - \frac{\alpha P d^4}{E h^3} \tag{6-13}$$

Again, we assume the temperature dependence of diaphragm side length expressed by equation 6-12 and negligible temperature dependence for diaphragm thickness. When the operation temperature increases from 25 °C to 600 °C, the side length increases from 300 μm to 300.5 μm according equation 6-12. However, temperature has significant effect on Young's modulus E of a material. Yet by now, there is no explicit analytical expression for the dependence of Young's modulus on temperature for silicon to the author's knowledge. The value of Young's modulus of silicon decreases with temperature, as being the case for all other materials. In general, its temperature dependence can be expressed as

$$E(T) = 190 \times 10^9 - \beta \Delta T \qquad (\text{Pa})$$

where β is a constant. We can make a reasonable assumption, letting $\beta = 70 \times 10^6\,\text{Pa}/°\text{C}$. This means that at 600 °C, the value of its Young's modulus will be decreased by one fourth of its room temperature value. This is quite reasonable.

By substituting d(T) expressed in equation 6-12 and E(T) expressed above into g in equation 6-13, and then using equation 6-1, the dependence of output voltage on temperature can be calculated. The results are depicted in figure 6.8 for temperature range from -20°C to 600 °C. The values of current and frequency used in this calculation are assumed the same as those used in other chapters. It is seen that when the temperature increases, the output voltage increases at the same pressure. This is due to the increase in diaphragm deflection with temperature. At low pressures, the temperature effects are not so pronounced. Yet at high pressures, the temperature effects becomes significant. At 300

kPa, the output voltage at -20 °C is 157 mV. It becomes 240 mV at 600 °C. The variation in output voltage is 80 mV. The dynamic output voltage range is 120 mV at room temperature. The variation with temperature is significant comparing with the dynamic output range. However, if the sensor is aimed to operate in pressure range between 0 kPa and 200 kPa, the variation in output voltage is 20 mV, half the value of the dynamic output range at room temperature. The compensating circuitry is needed depending on specific applications.

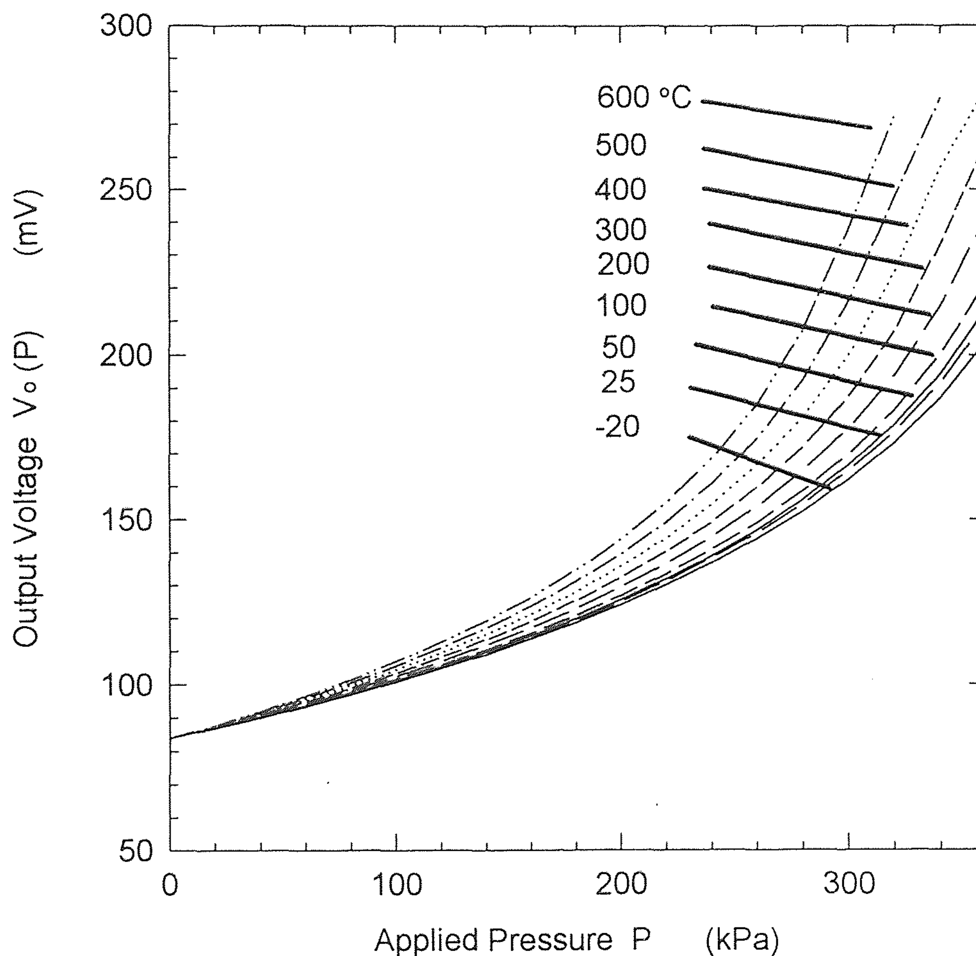

Figure 6.8. Output voltage V versus applied pressure differential

CHAPTER 7

PHYSICAL DESIGN OF THE SENSOR DEVICE

The previous chapters have developed the electromechanical principles for the sensor design. In this chapter, we will discuss the physical design based on the established principles in the previous chapters. The high temperature pressure sensor is based on the wafer fusion bonding process and anistropic wet chemical etching technology. Therefore, this is a two-wafer processing: handle wafer and top wafer. The mask designs are done on the IC station of the MENTOR GRAPHICS version 8.2.

7.1 Handle Wafer Masks Design

There are two masks for the handle wafer processing. The first mask is the cavity patterning one as shown in figure A.1 in appendix A.

The edge length of the square diaphragm is 300 μm. This edge length is chosen to get reasonable output voltage as we have already discussed before. On this MASK, an alignment mark is designed for the alignment of the second mask to the first one.

The second mask for the handle wafer processing is the primary coil definition, as shown is figure A.2. Nine turns are designed on this level. The contact pads(wire bonding pads) are automatically formed at the same time the primary coil is defined, as shown also in the figure.

The size of the bonding pads is $100 \times 100\ \mu m^2$. On this mask, two alignment marks are designed. One is used to align the first level, and appeared to be a hatch cross. The other one is a bigger cross, used as the alignment mark when the top wafer and handle wafer are aligned in the bonding process.

Figure A.3 shows the handle wafer pattern after the second mask is processed. It is shown in the figure that the primary coil sits in the center of the cavity, which is 36 μm

wider on each side than the coil edge. The reason to design the coil in the center and leave 36 μm spacing between the coil edge and the cavity edge is to get a more uniform deflection in the coil area and a more linear response to applied pressure, which will be discussed later in this chapter.

7.2 Top Wafer Masks Design

There also two masks for the top wafer processing. The first mask involves the definition of the diaphragm dimension. On this mask, the bright square field, shown in the figure A.4, is used to define the boron diffusion windows, which is 100 μm lager on each side than the true deflect diaphragm. The rim area beyond the diaphragm is used as the wire bonding areas to the handle wafer. An align mark (cross) is designed on this mask for the alignment of the second mask.

The second mask for the top wafer processing is a coil definition mask which is similar to the second mask for the handle wafer, as shown in figure A.5. Two align marks are appeared on this mask. One is for the alignment to the first one, the other is used to align the handle wafer for wafer bonding.

Figure A.6 plots out the top wafer pattern after the second mask is processed. As we mentioned before, the primary coil sits in the center on the cavity and the secondary coil in the center of the diaphragm. After the handle wafer and the top wafer are bonded together, the two coils directly face to each other. It is designed such that it gives the best coupling between the two coils and the largest output voltage.

We recall that the magnetic flux concentrates mainly to the area very close to the coil, and decreases quickly with the distance away from the coil. The flux contribution of one turn in the other tends to reduce the total magnetic flux in the coil. Therefore, the displacement from the symmetrical lay-out between the two coils is undesirable.

The deflection of the edge-fixed diaphragm is usually non-uniform and non-linear in response to an applied pressure, especially in the area close to the diaphragm edge.

However, the deflection in the center area in more linear than that in the edge area. If there is enough spacing between the "active"(coil) area and the edge, the deflection of the coil area can generally be treated uniform. This reflects a more linear output.

Finally, in figure A.7, a complete sensor chipgraphy is depicted after the completion of the full mask processing. The cross sectional view of the sensor was shown in figure 3.1.

For the sake of comparison, different sized sensors from 100 μm to 400 μm edge length are also designed, as appeared in figure A.7.

CHAPTER 8

SENSOR FABRICATION

In this chapter, sensor fabrication will be presented. Some key processing steps such as boron diffusion and KOH etching for diaphragm formation will be discussed in detail. This is two-wafer processing: handle wafer and top wafer processing.

8.1 Device Processing

The sensor fabrication starts with double polished (100) n-Si wafers. It is done first by oxidizing the silicon wafers to get a oxide thickness of 1 μm. Then the cavity window is opened by photolithography on the handle wafer and a boron diffusion window on the top wafer. After the cavity is etched 2 μm down to the handle wafer by KOH solution and boron is heavily doped 5 μm deep into the top wafer, metal is sputter deposited on to both the handle wafer and top wafer. Primary and secondary coils are defined by lithography and buffered HF etching. This is followed by sputtering a layer of Pyrex glass onto the top wafer. The two wafers are then aligned and bonded by heating them to above 800 °C for 30 minutes. After the backside etch by KOH of the top wafer, and pads reveal by buffered HF, sensor chips are realized. A full processing flow is presented in appendix B.

8.2 Discussions of Some Critical Processing Steps

8.2.1 Silicon Wafer Bonding

Silicon-silicon bonding has growing importance for silicon-on-insulator processing[25], wafer-scale packaging[26], and silicon micromechanical sensors, actuators and other microstructures[27]. The silicon wafer bonding was firstly presented by Lasky in 1985[28] as an alternative method for the fabrication of SOI devices. As the sensor and transducer

technologies march on, there are increasing interests in the investigations on silicon wafer bonding. Extensive work has been done to develop various bonding techniques for silicon micromechanical sensors. There were very good review papers for silicon wafer bonding techniques[29-31].

Basically, silicon direct bonding with or without thermal oxide usually requires high temperatures above 1000 °C. High temperature operation will cause carriers re-distribution and therefore modify the device properties. This is true for piezoresistive-type sensors. Further more, this technique is applicable to wafers with flat surfaces. If this technique has to be chosen, the surface needs to be treated for good bonding.

Another widely investigated wafer bonding technique is based on some kinds of low temperature glass as an intermediate layer by applying or without applying the external field. If an external electrical field is applied, it is called anodic bonding. However, anodic bonding is usually possible only when at least one wafer is not oxidized and applicable generally to the bonding of two wafers with flat surfaces. If oxide is grown on one or both wafers, and one wafer or both wafers are patterned , anodic bonding is not applicable. In this case, silicon fusion bonding based on an intermediate layer has to be used.

Specific bonding technique should be chosen according to specific applications. In this thesis, neither silicon direct bonding nor anodic bonding is applicable because both wafers have oxide on them and both wafers are patterned in our case. Therefore, silicon fusion bonding is used with the help of a glass as an intermediate layer.

When used as an intermediate layer, the glass should satisfy some requirements such as thermal match, sealing temperature, and glass form that determines the specific processing technique. In table 8-1, the basic properties are listed for some glasses which could be considered as low temperature sealing applications.

Table 8.1 The basic properties of some glasses for low temperature silicon wafer bonding applications

Glass type	Thermal expansion x 10^{-6}/K (0-300°C)	Softening point °C , $10^{7.6}$ poise	Sealing Temp. °C	Max. service Temp. °C
7070*	3.20		1025	431
7574*	3.40	644	750	725
7723*	3.50	770	810	455
9108*	5.32	742	950	471
9119*	5.30	754	950	440
G017-002#	3.6	650	700	
G017-344#	4.3	600	650	
G017-339#	4.7	370	450	
7740**		821	950	
7570**		440		

* Corning glass
\# Schottglas
**Iwaki Glass

The sensor described in this thesis is supposed to work at temperatures up to 600 °C, the glass should be stable at 600 °C. In this regard, Pyrex glass(#7740 Corning Glass Company) is chosen. Pyrex glass has thermal expansion of coefficient fairly close to that of silicon in a wide temperature range as we have discussed in chapter 6. Pyrex glass has a softening point of 820 °C, and melting point of around 1050 °C. The bonding temperature must exceed the softening point. 950 °C is suggested by Corning Glass Company as sealing temperature.

The bonding is done by firstly sputtering a thin layer of Pyrex glass(1-2 μm) on to one of the two patterned wafer, then the two wafers are carefully aligned and held in place and the attached wafer-pair is put into furnace at 950 °C for 15 minutes with the presence of oxygen. In this step, it is important to hold the wafer-pair in alignment, because

displacement may occur after the glass is melted and it will fail the all efforts in the foregoing device fabrication.

8.2.2 Backside Etch of Top Wafer

Technically, there are two major technologies for etching silicon. One is wet etching and the other is dry etching. Wet etching can further be divided into chemical etching and electrochemical etching. Both chemical and electrochemical etching are widely used methods in the micromechanic fabrications. Dry etching such as reactive ion etching(RIE) and plasma etching are routinely used in IC processing and are being introduced into micromechanical fabrications. Dry etching, However, generally gives rough etching surfaces, especially with deep dry etching. Therefore, anistropical wet etching is the most widely used method for silicon microfabrication[32].

The most widely used etchant are KOH, EPW and TMAH. The former is less toxic and can give a very good etch surface if properly handled in etching processing. The disadvantage is that KOH also has large etch rate for silicon dioxide and metals. Etchant EPW has a very low etch rate for silicon dioxide and metals, but it is very toxicating and needs special handling in etching process. In this thesis, KOH is suggested for both cavity and backside etching of the top wafer in two reasons: 1) KOH solution is the least toxicating etchant and needs no special handling, and 2) the etching can be easily performed and controlled. In our case, silicon dioxide is removed from the whole backside surface of the top wafer, pattern protection is not needed, the back surface of the handle wafer is protected by a thin layer of silicon nitride film. KOH etches silicon nitride very slowly compared with silicon. Therefore, the fast etching rate of SiO_2 is not critical in the etching process. The diaphragm thickness is controlled by a heavy boron diffusion which acts as an etch stop.

CHAPTER 9

EXPERIMENTS ON ALUMINUM FOIL COILS

In order to best understand the sensor performance, scaling experiments are done based on aluminum foil coils. In this regard, different glass layers are sandwiched between the different sized coils for the simulation of the real device performance. The experiment are based on a 200 μm × 200 μm diaphragm and 6 turn-coil device. So the aluminum foil coils are made 500, 1250, 2500 and 5000 times the micromachined coils, respectively. The coil line width, turn pitches and coil gaps are also enlarged accordingly. The specific parameters are listed in the following:

Coil Parameter	Real coil μm	500× coil mm	1250× coil mm	2500× coil mm	5000×coil mm
a	4	2	5	10	20
b	8	4	10	20	40
g	2	1	2.5	5	10
coil pitch	8	4	10	20	40

The experiment results are shown in figure 9.1 for the zero pressure differential case. The plotted line is the best fit to single layer metal the experimental results. One result from a double level metal coil is also shown (with a triangle point) for comparison. It can be seen that the output voltage per unit current per MHz increases as the dimension increases. The experimental points fit fairly well in a straight line. The double level coil shows a 4× lager output. The output voltage of the sensor scales approximately propotional to the physical scaling factor.

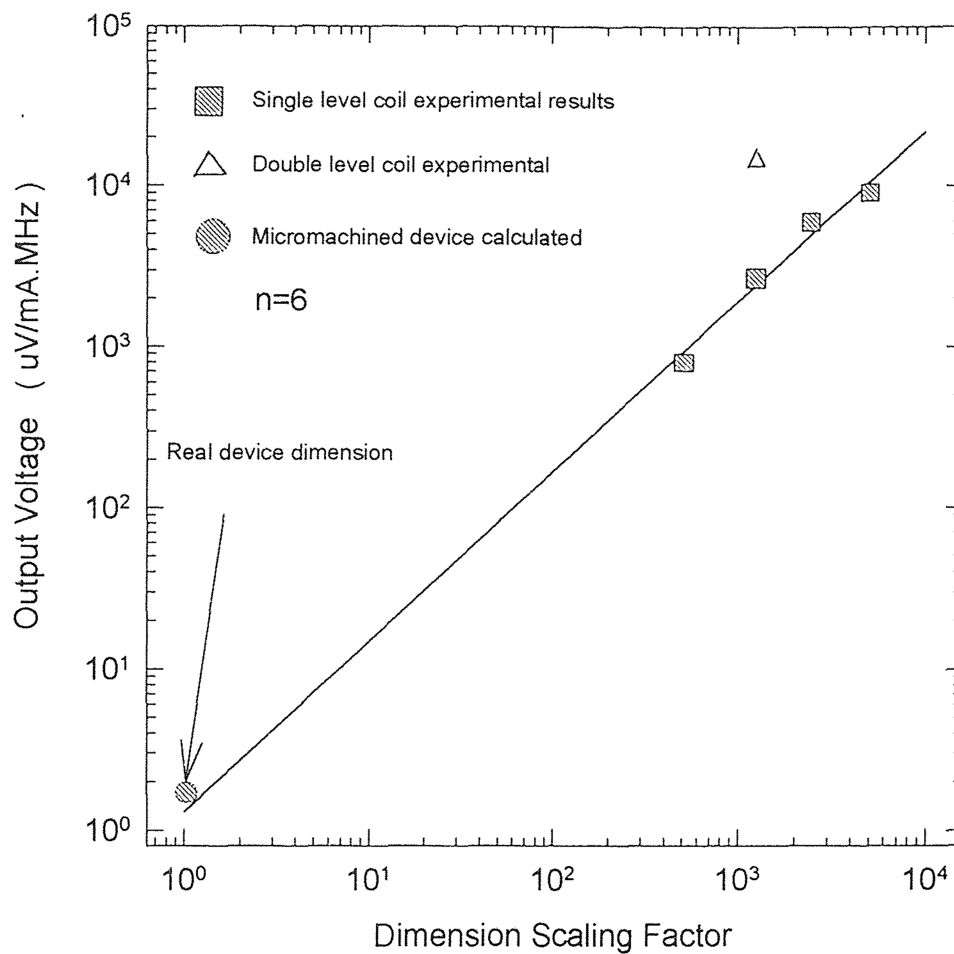

Figure 9.1 Sensor device dimension scaling experiments. The calculation result for a 6 turn device is shown as indicated. The other four points represent the outputs from the aluminum foil coils of 500, 1250, 2500 and 5000 times of the real device dimension. One experimental result for double level coil device is also shown for comparison.

CHAPTER 10

CONCLUSIONS

This thesis presents the design for a high temperature pressure sensor. The design is based on the electromagnetic induction principle and silicon micromachining technology. Silicon pressure sensors based on this design can be operated at temperatures up to 600°C if appropriate conductor and adhesive materials are chosen. Modeling predicts an output voltage span of 78 mV at room temperature with an applied alternate current amplitude of 100 mA and frequency of 200 MHz for a sensor with diaphragm dimension of 300 μm× 300 μm and thickness of 5 μm and pressure range of 0- 400 kPa, and single layer coils. This output voltage is moderately high for practical applications. The sensitivity and dynamic range of these sensors can be varied over a large range by changing the diaphragm thickness and area. Higher output and lower frequency are possible with multiple level primary and/or secondary coils. Experiments on aluminum foil coils confirm that the sensor's output can be increased by designing double level or multilevel metal coils.

Device processing is proposed in detail. Wafer bonding and backside etching for diaphragm formation are the two major steps in realizing a full device and are discussed in detail. Platinum silicide is adopted as coil material to attain high temperature operation. Pyrex glass is proposed as an adhesive bond material for the intermediate layer between wafers because it provides a fairly good thermal match with silicon over a wide range of temperatures from -20 °C to 500 °C. In this thesis, the cavity must be sealed in a vacuum in order to reduce the effects of residual gas within the sealed cavity.

This thesis concludes that a magnetic coupled silicon pressure sensor is feasible for operation up to 500 °C.

APPENDIX A

MASK LAYOUT

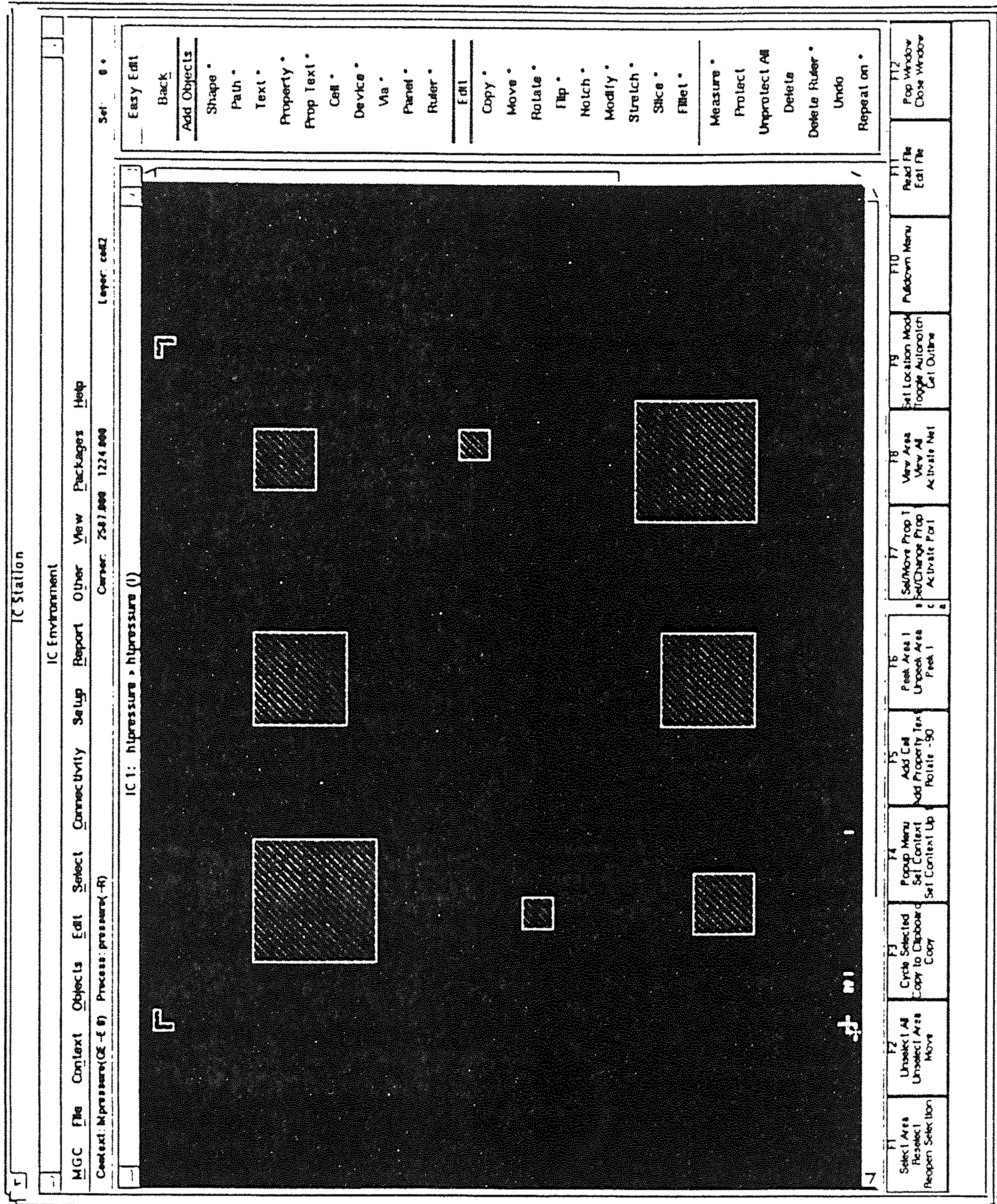

Figure A.1. The first mask for cavity definition on handle wafer

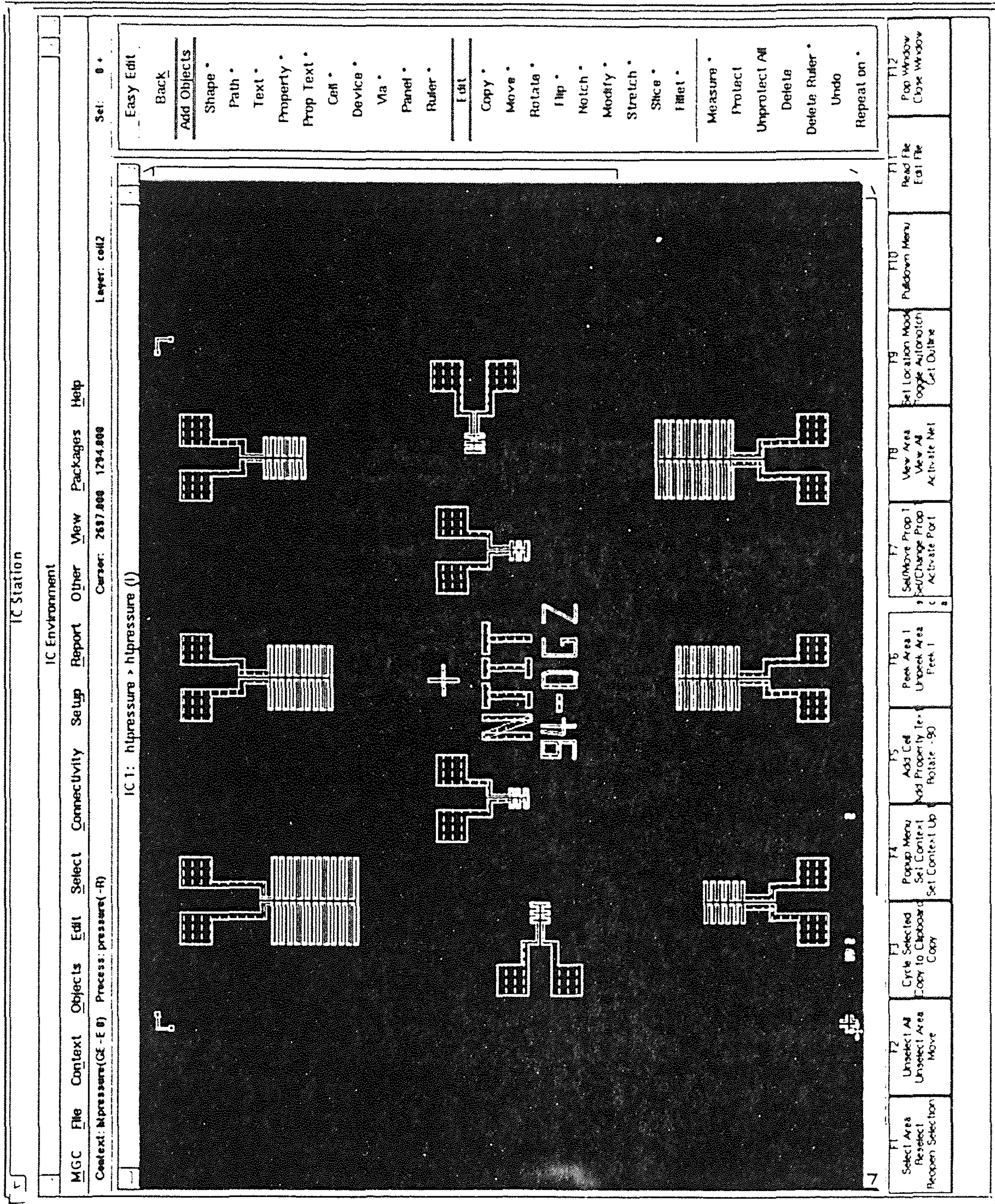

Figure A.2 Mask for primary coil definition on handle wafer

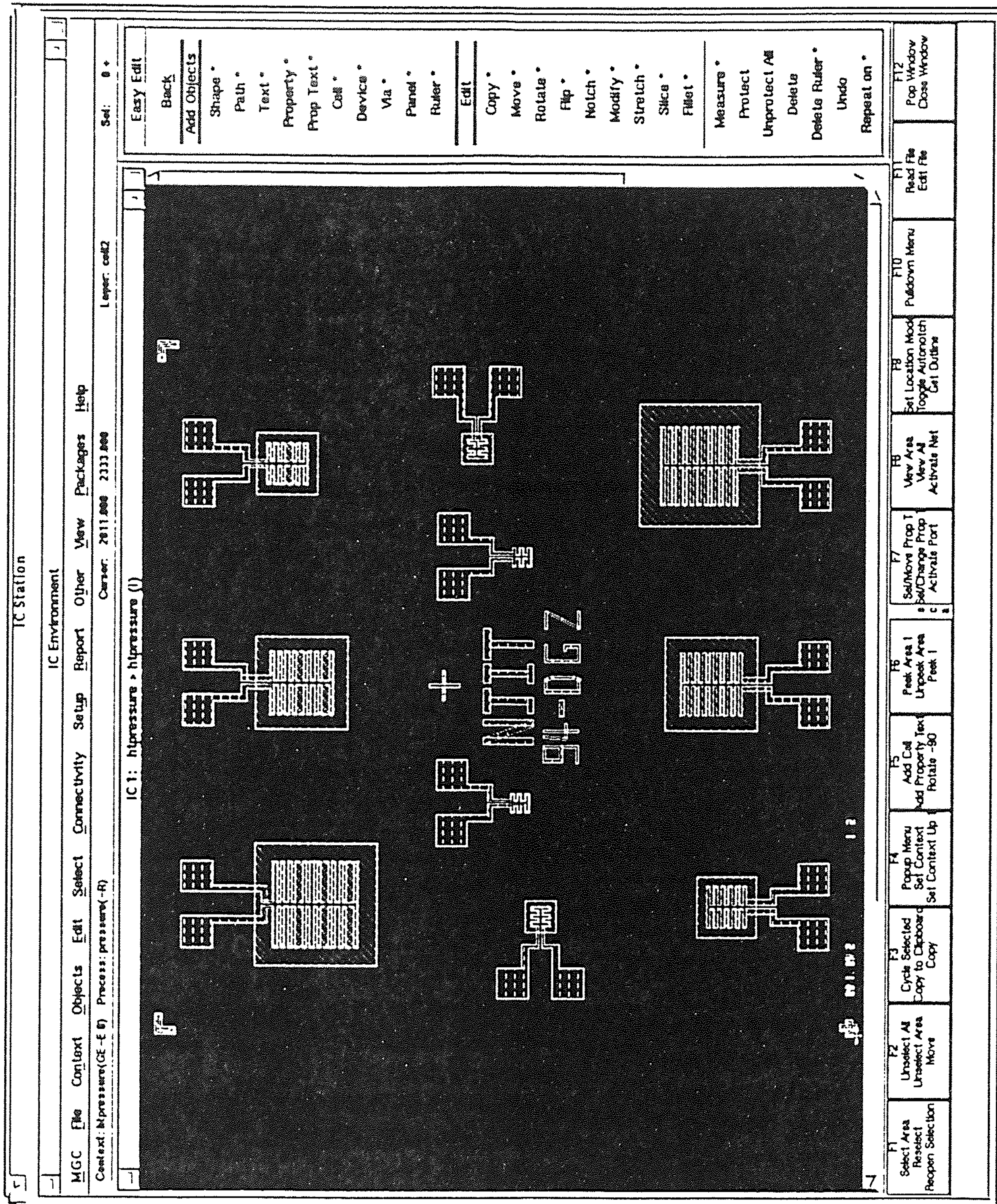

Figure A.3 Device pattern on the handle wafer after the processing of primary coil etching

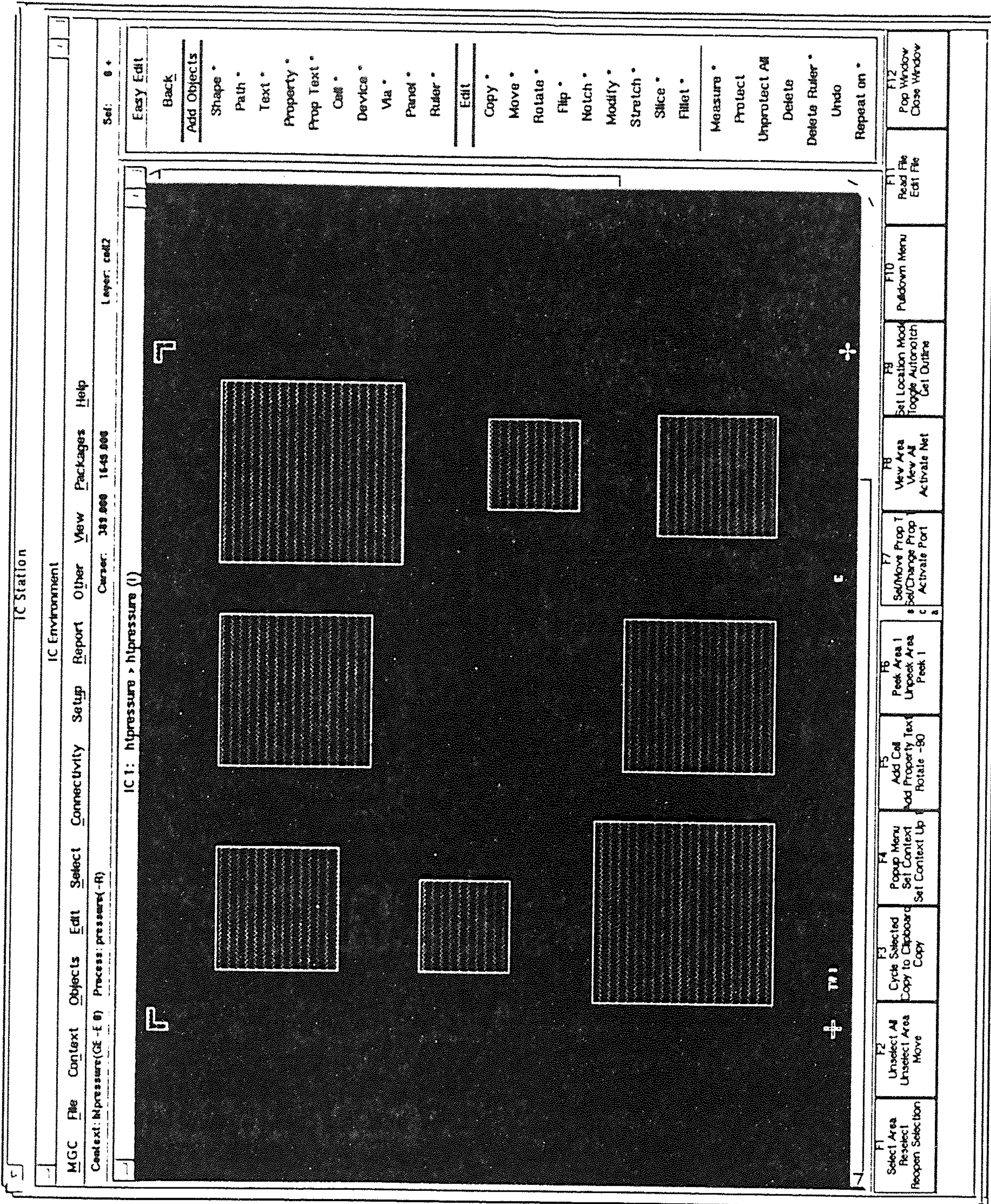

Figure A.4 Boron diffusion mask for the definition of diaphragm area

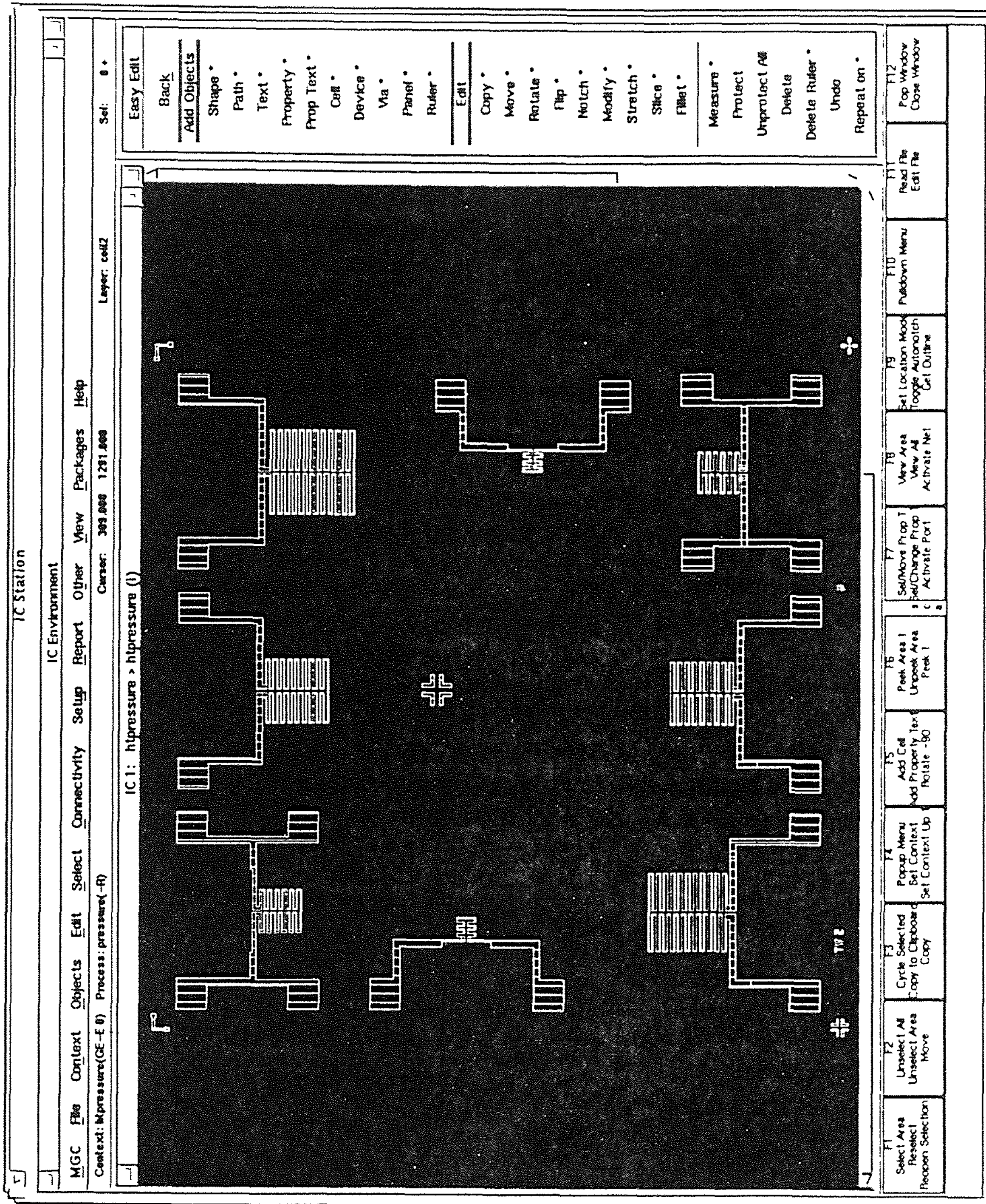

Figure A.5 Secondary coil definition mask

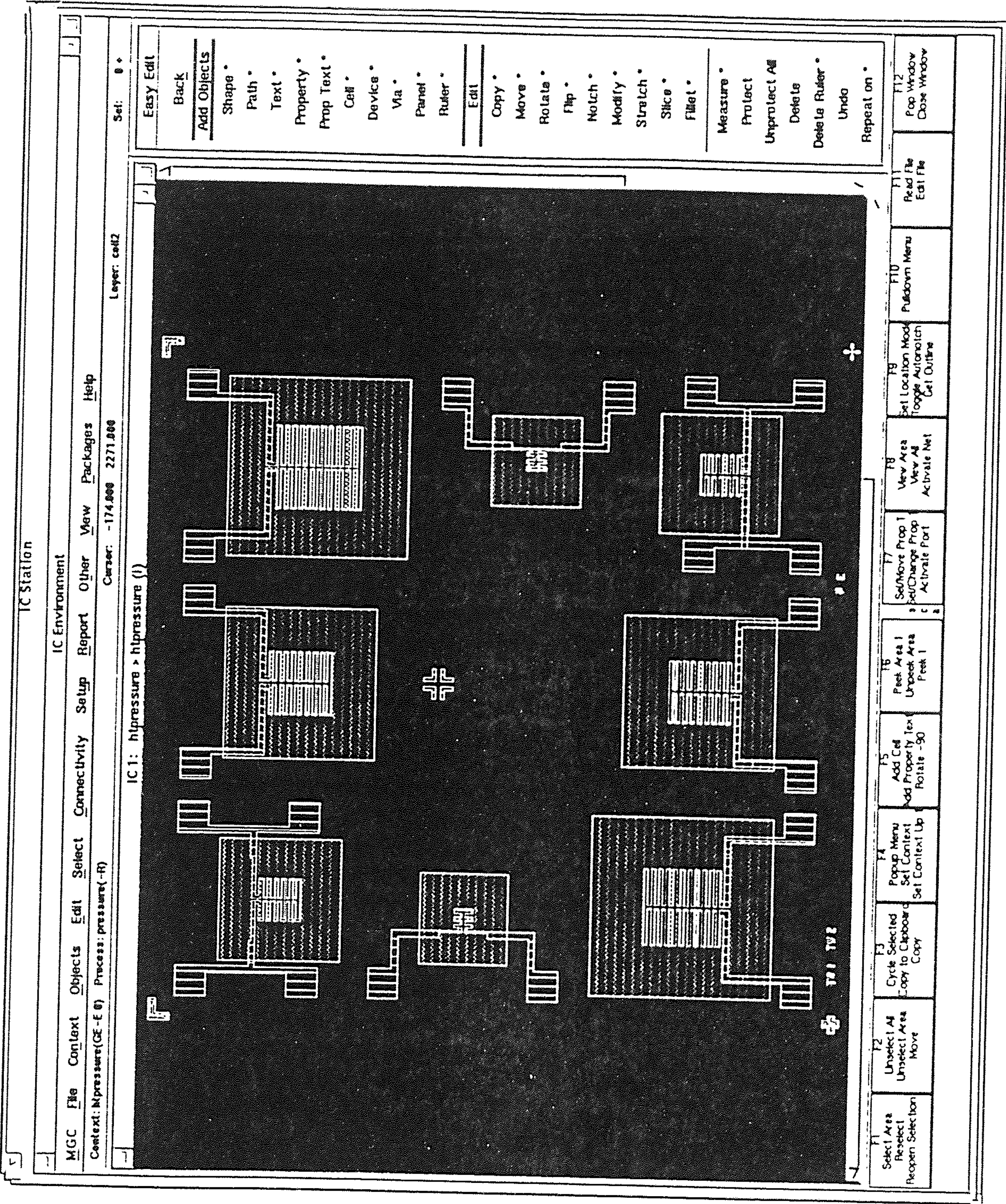

Figure A.6 Pattern layout on the top wafer after secondary coil defined

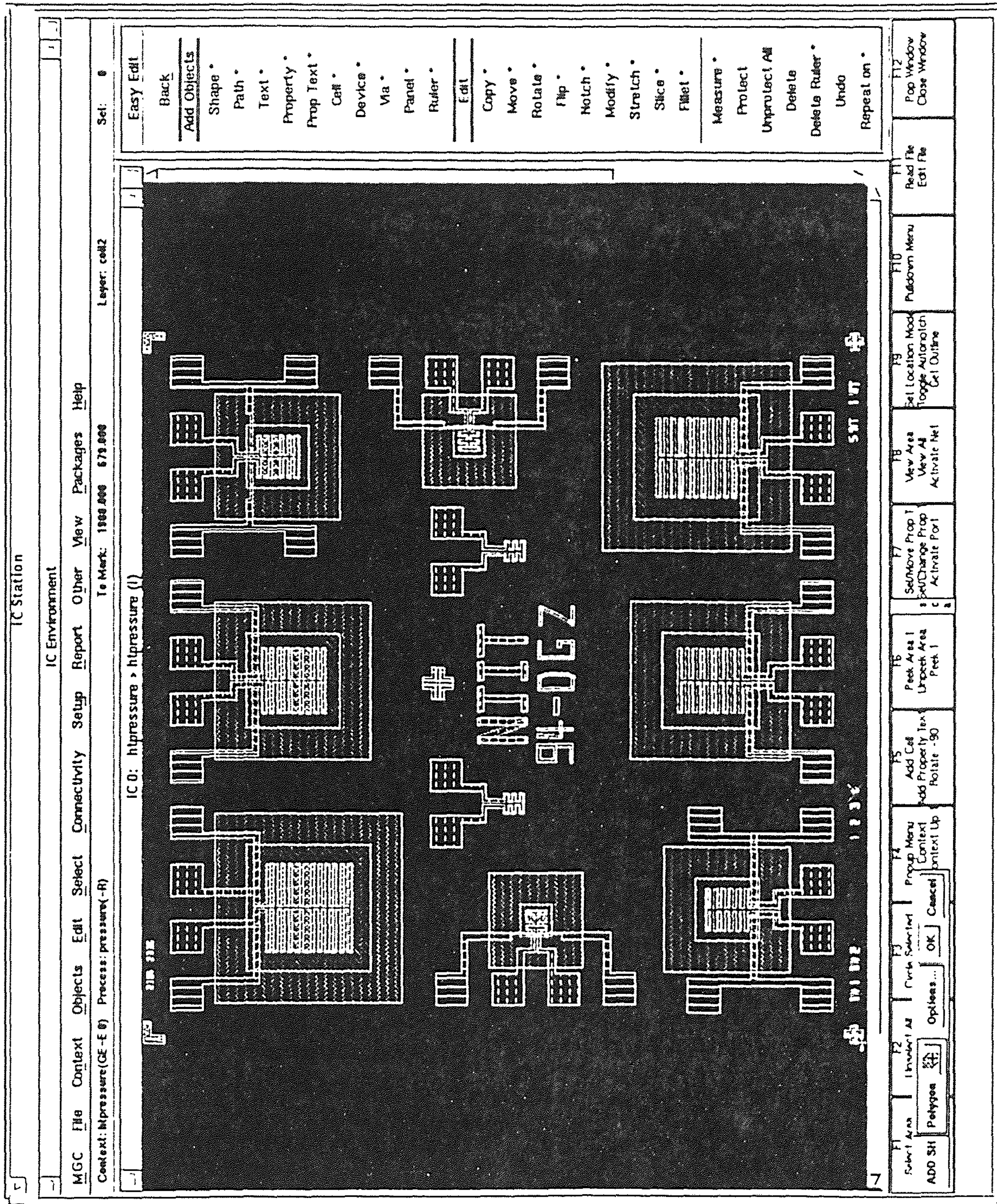

Figure A.7 The pattern layout for the whole device chip after the completion of device processing

APPENDIX B

SENSOR FABRICATION PROCESS FLOW

1. Handle Wafer Processing Steps

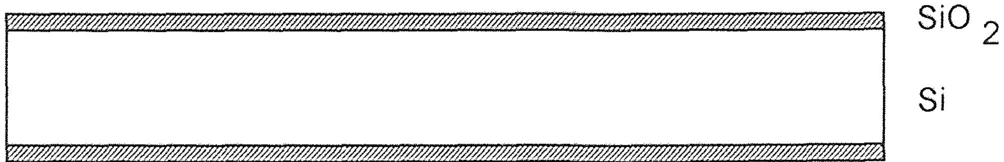

1. Wafer cleaning and oxidation

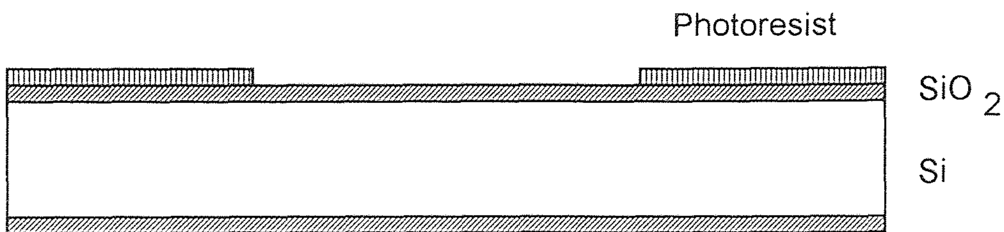

2. Photolithography(Cavity definition (mask 1))

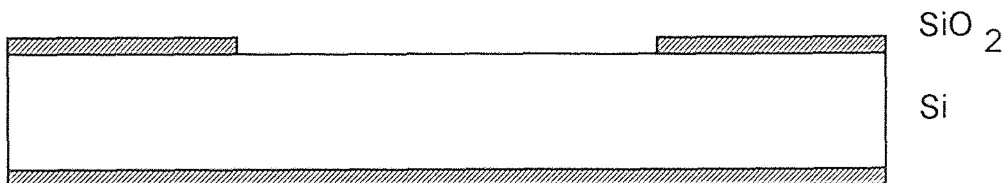

3. Oxide etch

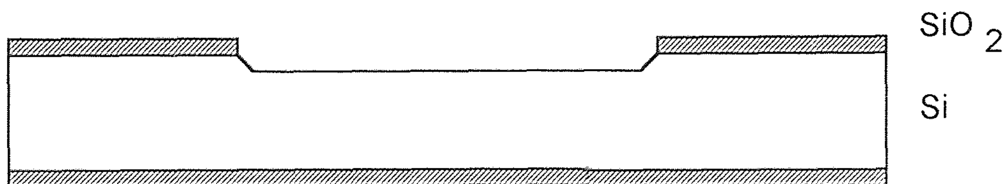

4. Cavity etch

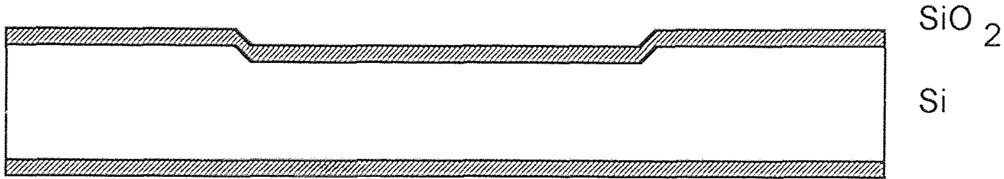

5. Wafer re-oxidation

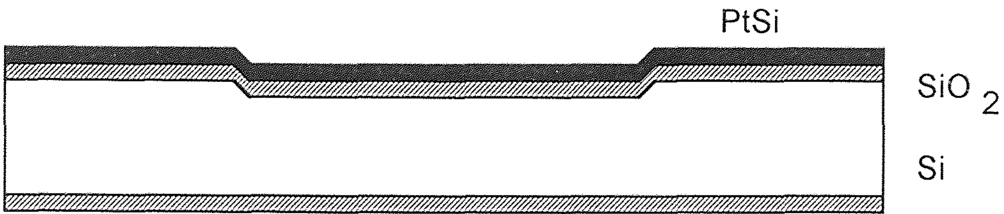

6. Coil metal deposition (Platinum silicide)

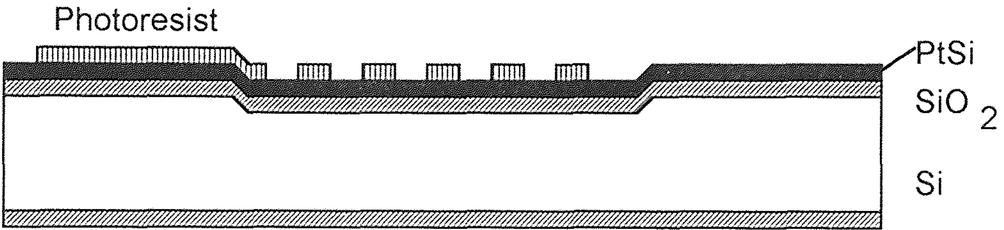

7. Primary coil definition(Mask 2)

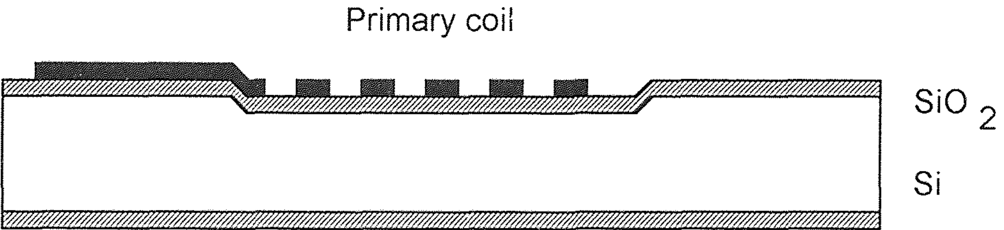

8. Platinum silicide etch

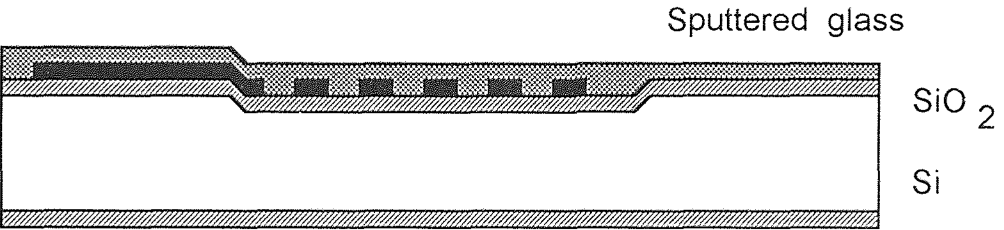

9. Glass deposition(Sputtering)

2. Top Wafer Processing

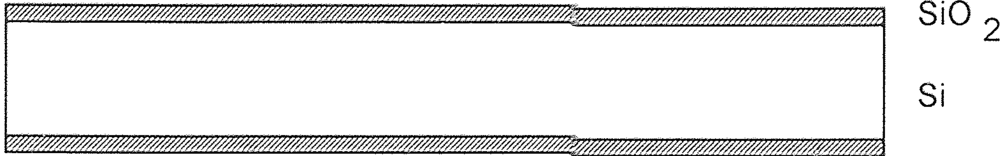

1. Wafer cleaning and oxidation

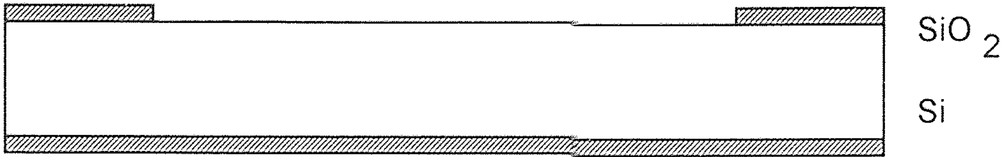

2. Diaphragm definition

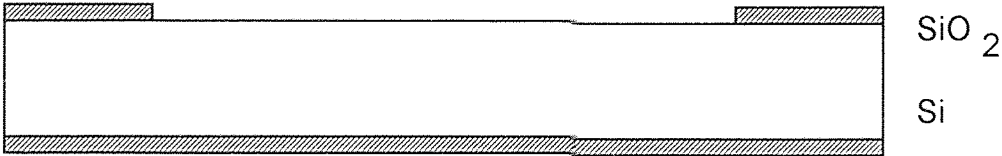

3. Oxide etch

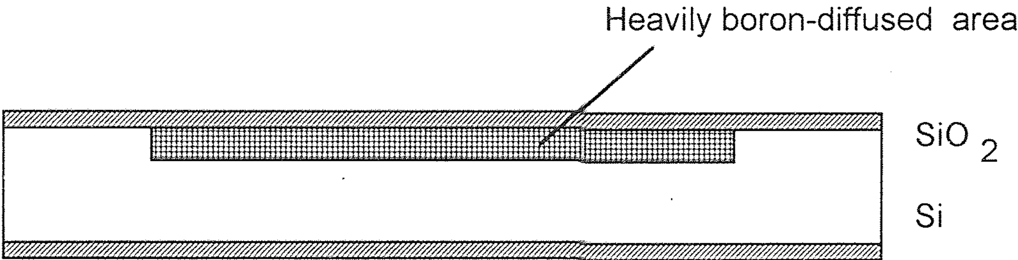

4. Boron diffusion

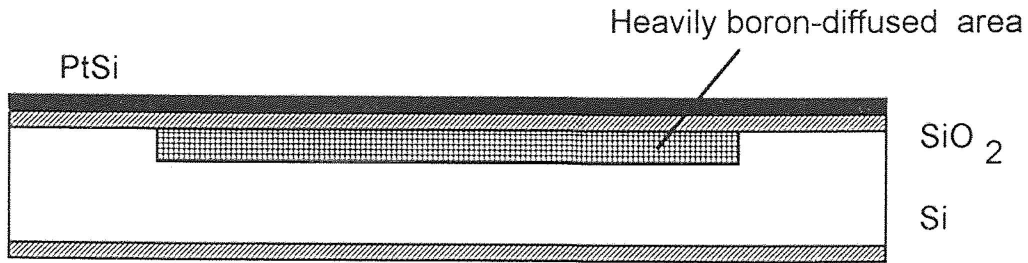

5. Coil metal sputtering

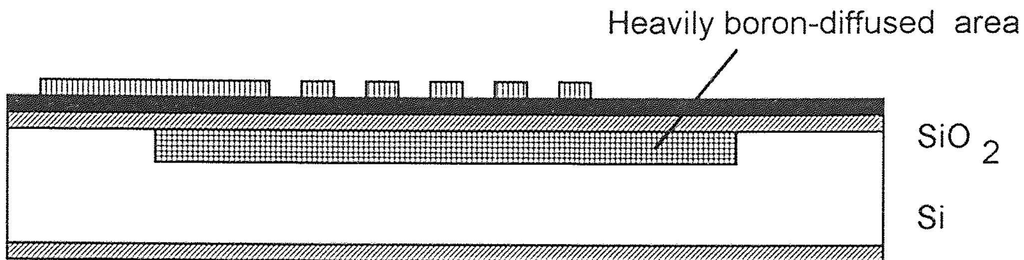

6. Secondary coil definition (Same as that for handle wafer)

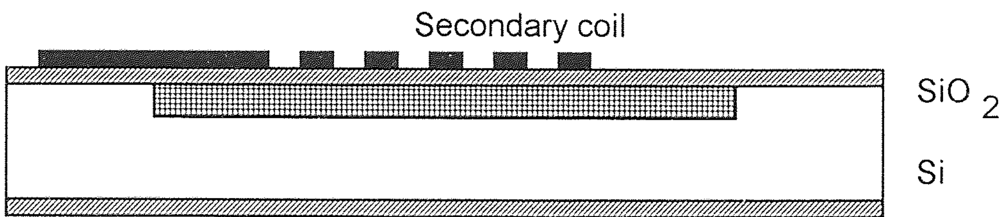

7. Platinum silicide etching

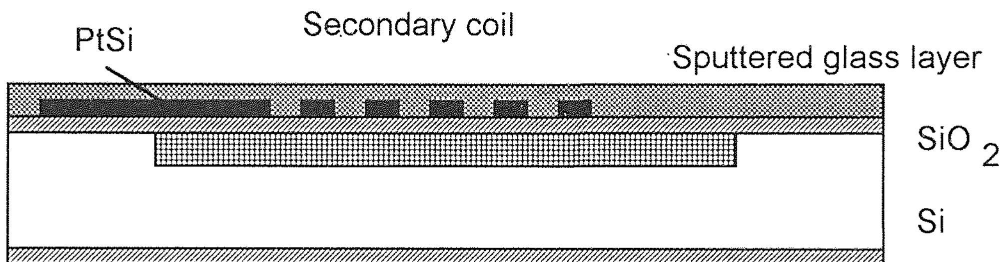

8. Sputter glass layer

3. Double Wafer Processing

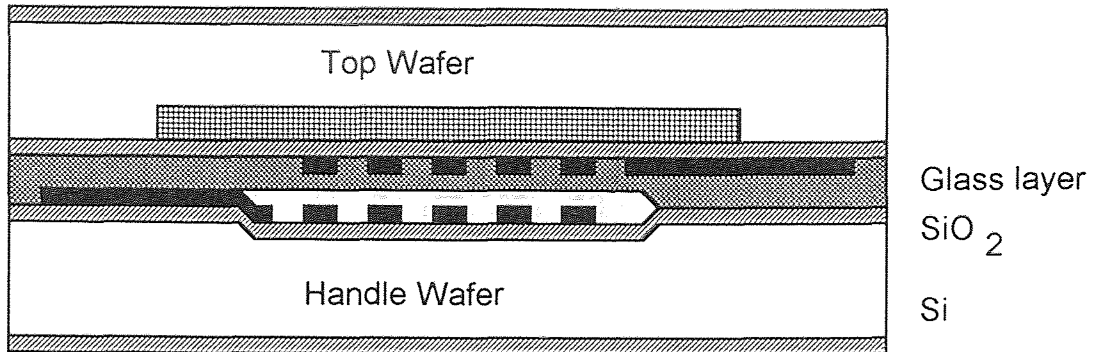

1. Wafer bonding

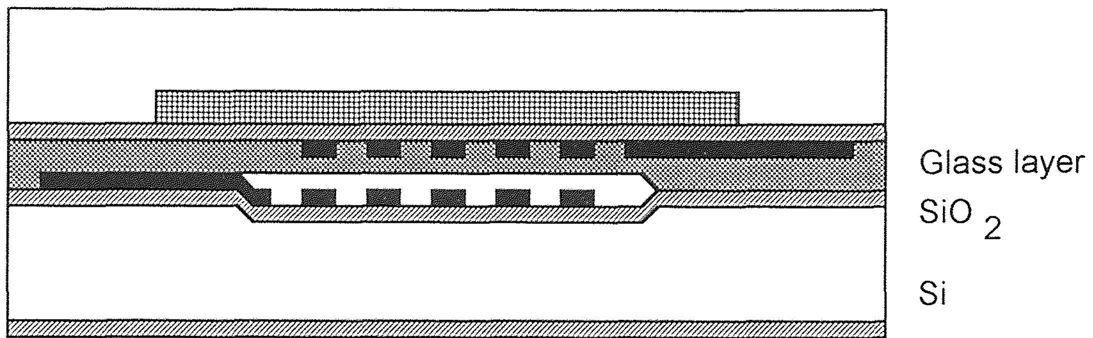

2. Remove oxide from the backside of the top wafer

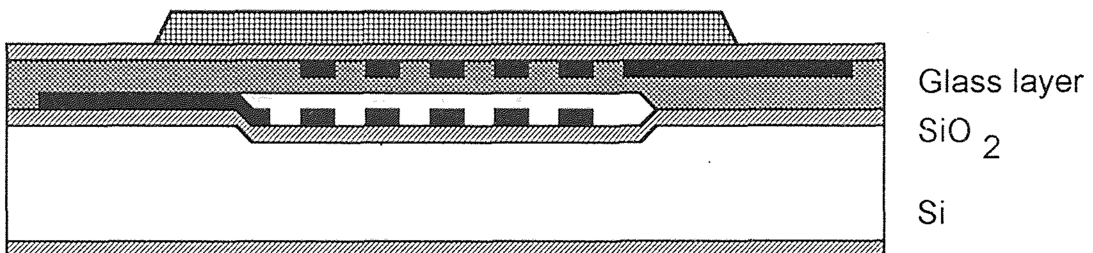

3. Backside etching silicon of the top wafer

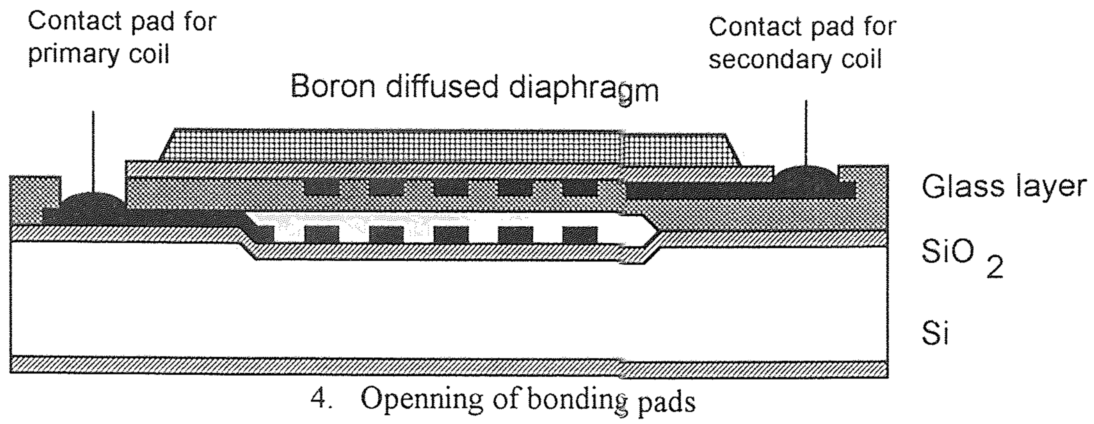

4. Openning of bonding pads

REFERENCE

[1] K. Peterson, "Silicon as a mechanical material", *Proceedings of IEEE.*, **7**, 420(1982)

[2] S.K.Clark and K.D.Wise, "Pressure sensitivity in anistropically etched thin-diaphragm pressure sensors", *IEEE Trans. Electron Devices*, **26**, 1887(1979)

[3] S. C. Kim and K. D. Wise, " Temperature sensitivity in silicon piezoresistive pressure transducers" *IEEE Trans. Electron Devices*, **30**, 802(1983)

[4] W. H. Ko, "Solid state capacitive pressure transducers", *Sensors & Transducers*, **10,** 304(1986)

[5] Y. Zhang and K. D. Wise, "A ultra sensitive capacitive pressure sensor with a bossed dielectric diaphragm", *Solid-State Sensor & Actuator Workshop*, Hilton Head, S. Carolina, June 13, 205(1994)

[6] K. Peterson, F. Pourahmadi, J. Brown, P. Parsons, M. Skinner, and J. Tudor, "Resonant beam pressure sensor fabrication with silicon fusion bonding", *Transducers' 91*, 664(1991)

[7] D. W. Burns, J. D. Zook, R. D. Horning, W. R. Herd, and H. Guckel, "A digital pressure sensor based on resonant microbeams", *Solid-State Sensor & Actuator Workshop*, Hilton Head, S. Carolina, June 13, 221(1994)

[8] C.Yeh and K. Najafi, "Bulk-silicon tunneling-based pressure sensors", *Solid-State Sensor and Actuator Workshop*, Hilton head, S. Carolina, June 13, 201(1994)

[9] P. J. French, S. R. Stiftser, F. R. White, and J. R. Abernathy, "Silicon-on-insulator(SOI) by bonding and etch-back", *IEEE IEDM Tech. Dig.*, 684(1985)

[10] K. Peterson, J. Brown, P. W. Barth, J. Mallon, and J. Bryzek, "Ultra-stable high temperature pressure sensors using silicon fusion bonding". *Transducers'91*, 90(1991)

[11] G. Chung, S. Kawahito, M. Ashiki, M Ishida, and T. Nakamura, "Novel high temperature pressure sensors using double SOI structures, *Transducers'91*, 676(1991)

[12] E. Obermeier, "Polysilicon layers lead to a new generation of pressure sensors", *Transducers'85*, 430(1985)

[13] Y. Lee, H. Seo, M. Arai, M. Ishida, S. Kawahito, and T. Nakamura, "High temperature pressure sensor using double SOI structures with two Al_2O_3 films", *The 7th Int. Conf. on Solid-State Sensors & Actuators*, 624(1993)

[14] OMEGA, *The Pressure Strain and Force Handbook*, OMEGA Engineering, J-14, (1982)

[15] W.S. Graber, "Low air pressure sensing on a chip", *Sensors*, June, 36(1993)

[16] R.H.Johnson, S.Karbassi, U.Scridar and B. Speldrich, "A high-sensitivity ribbed and bossed pressure sensor", *Sensors & Actuators* *A*35, 93(1993)

[17] K.M.Mahmound, R.P.Van Kampen, M.J.Rutka and R.F.Wolffenbuttel, "A silicon integrated smart pressure sensor", *The 7th Int. Conf. on Solid State Sensors and Actuators*, 217(1993)

[18] Y.Wang, L. Liu, X. Zheng and Z. Li, "A novel pressure sensor structure for integrated sensors", *Sensors & Actuators* **A21-23,** 62(1990)

[19] S. Timoshenko and S. Woinowski-Krieger, *Theory of Plates and Shells*, 2nd Edition, New York, McGraw-Hill Book Company, 402(1959)

[20] M. Ohring, *The Material Science and Thin Film*, New York, Academic Press, 414(1982)

[21] Motorola, Inc., Pressure Sensors 1992, Application Note: 27

[22] S.M.Sze, *VLSI Technology*, New York, McGraw-Hill Book Company, 375(1983)

[23] G.E.McGuire, *Semiconductor materials and process technical handbook*, New York, McGraw-Hill Book Company, 575(1988)

[24] S.Timoshenko, *J. Opt. Soc. Am.*, **11,** 233(1925)

[25] R. Black, S. Arthur, R. Gilmore, N. Lewis, E. Hall, and R. Lillquist, "Silicon and silicon dioxide thermal bonding for silicon-on-insulator applications", *J. Appl. Phys.*, **63,** 2773(1988)

[26] S. Shoji and M. Esashi, "Micro-pump for integrated chemical analyzing systems", *Tech. Digest, 7th Sensor Symp.* Tokyo, Japan, May, 217(1988)

[27] K. Peterson, P. Barth, J. Poydock, J. Brown, J. Mallon, Jr. and J. Bryzek, "Silicon fusion bonding for pressure sensors", *Solid-State Sensor and Actuator Workshop*, Hilton Head Island, SC, U.S.A., June 6-9, 144(1988)

[28] J.B. Lasky, "Wafer bonding for silicon-on-insulator technologies", *Appl. Phys. Lett.*, **48**, 78(1986)

[29] W.H. Ko, J.T. Suminto and G.J, yeh, "Bonding techniques for microsensors", *Micromachining and Micropackging of Transducers*, 198 (1985)

[30] P.W. Barth, "Silicon fusion bonding for fabrication of sensors, actuators and microstructures", *Sensors & Actuators*, **A21-A23,** 919(1990)

[31] A. Hanneborg, "Silicon wafer bonding techniques for assembly of micromechanical elements", *Proceedings IEEE MEMS Conference,* Nara, Japan, Jan. 1-Feb. 2, 92(1991)

[32] H. Seidel, L. Csepregi, A. Heuberger and H. Baumgartel, "Anistropical etching of crystalline silicon in alkaline solutions", *J. Electrochem. Soc.*, **137**, 3613(1990)

[33] R. Okojie, "A high-temperature pressure sensor utilizing linear voltage differential transformer(LVDT) and silicon wafer-to-wafer fusion bonding technologies", Master's Thesis, Department of Electrical and Computer Engineering, New Jersey Institute of Technology, 1993